REALTIME MAGNETOMETER CALIBRATION FOR SPINNING AEROSPACE VEHICLES

A THESIS SUBMITTED TO
THE GRADUATE SCHOOL OF NATURAL AND APPLIED SCIENCES
OF
MIDDLE EAST TECHNICAL UNIVERSITY

BY

MUSTAFA EFE ÇETIN

IN PARTIAL FULFILLMENT OF THE REQUIREMENTS
FOR
THE DEGREE OF MASTER OF SCIENCE
IN
AEROSPACE ENGINEERING

FEBRUARY 2022

Approval of the thesis:

REALTIME MAGNETOMETER CALIBRATION FOR SPINNING AEROSPACE VEHICLES

submitted by **MUSTAFA EFE ÇETIN** in partial fulfillment of the requirements for the degree of **Master of Science in Aerospace Engineering Department, Middle East Technical University** by,

Prof. Dr. Halil Kalıpçılar
Dean, Graduate School of **Natural and Applied Sciences** _____

Prof. Dr. Serkan Özgen
Head of Department, **Aerospace Engineering** _____

Assist. Prof. Dr. Halil Ersin Söken
Supervisor, **Aerospace Engineering** _____

Prof. Dr. Ozan Tekinalp
Co-supervisor, **Aerospace Engineering** _____

Examining Committee Members:

Assist. Prof. Dr. Ali Türker Kutay
Aerospace Engineering, METU _____

Assist. Prof. Dr. Halil Ersin Söken
Aerospace Engineering, METU _____

Prof. Dr. Ozan Tekinalp
Aerospace Engineering, METU _____

Prof. Dr. Umut Orguner
Electrical and Electronics Engineering, METU _____

Prof. Dr. Cengiz Hacızade
Aeronautical Engineering, ITU _____

Date: 08.02.2022

I hereby declare that all information in this document has been obtained and presented in accordance with academic rules and ethical conduct. I also declare that, as required by these rules and conduct, I have fully cited and referenced all material and results that are not original to this work.

Name, Surname: Mustafa Efe Çetin

Signature :

ABSTRACT

REALTIME MAGNETOMETER CALIBRATION FOR SPINNING AEROSPACE VEHICLES

Çetin, Mustafa Efe
M.S., Department of Aerospace Engineering
Supervisor: Assist. Prof. Dr. Halil Ersin Söken
Co-Supervisor: Prof. Dr. Ozan Tekinalp

February 2022, 67 pages

Magnetometers are essential sensors for attitude estimation application in small spacecrafts due to their robust, inexpensive and lightweight characteristics. However, their direct usage is not applicable due to sensor errors. These errors limit the overall attitude estimation accuracy. This study proposes a complete real-time attitude independent magnetometer calibration algorithm for spinning aerospace vehicles. The recursive algorithm aims estimating the complete error state; consisting bias, scale factor and misalignment corrections, in real-time and without requiring any attitude information. To build the algorithm the well-known attitude-independent observation that is based on the magnitude of the sensed magnetic field is aided with new introduced quasi-measurements. The algorithm is tested with both simulations and real spacecraft data. Four quasi-measurements, which are derived using dynamic characteristics and orbital properties of the aerospace vehicle, considerably improve the convergence characteristics and estimation accuracy of the filter.

Keywords: Magnetometer Calibration, Quasi-Measurements, Spinning Aerospace Vehicles, TWO-STEP, Unscented Kalman Filter

ÖZ

HAVA ARAÇLARI İÇİN GERÇEK ZAMANLI MANYETOMETRE KALİBRASYONU

Çetin, Mustafa Efe
Yüksek Lisans, Havacılık ve Uzay Mühendisliği Bölümü
Tez Yöneticisi: Dr. Öğr. Üyesi. Halil Ersin Söken
Ortak Tez Yöneticisi: Prof. Dr. Ozan Tekinalp

Şubat 2022 , 67 sayfa

Manyetometreler ucuz, hafif ve dayanıklı yapılarından dolayı küçük uzay araçlarındaki yönelim belirleme uygulamalarında yaygın şekilde kullanılmaktadır. Fakat doğrudan kullanımları sensör hataları sebebiyle mümkün değildir. Söz konusu hatalar ulaşılabilecek yönelim belirleme hassasiyetini kısıtlamaktadır. Ne var ki ardışık çözüm üreten özyinelemeli algoritmalar kullanılarak manyetometre hataları (sabit kayma hatası, ölçeklendirme hatası ve eksenel kaçıklık hataları) kestirilip, ölçümler düzeltilebilir. Bu çalışmada Türkçe fırdöndü uydu olarak tabir edebileceğimiz dönü (ing. spin) kararlı uydular için tüm hata uzayını kapsayacak şekilde, gerçek zamanlı ve yönelimden bağımsız manyetometre kalibrasyon algoritması önerilmektedir. Algoritma oluşturulurken genel olarak kullanılan yönelim bağımsız, ölçüm büyüklüğünü temel alan gözlem, fırdöndü uydu dinamiği ve yörünge bilgisi kullanılarak türetilmiş sözde ölçümlerle desteklenmiştir. Önerilen yöntemin başarımı sentetik olarak üretilmiş ve gerçek uzay aracından toplanmış ölçümlerle doğrulanmıştır. Dört sözde ölçüm eklenmesiyle filtrenin doğruluğu ve yakınsama hızı arttırılmıştır.

Anahtar Kelimeler: Manyetometre Kalibrasyonu, Sözde Ölçüm, Fırdöndü Uydular, İki Adımlı, Sezgisiz Kalman Filtresi

Inventas vitam iuvat excoluisse per artes...

ACKNOWLEDGMENTS

First and foremost, I wish to express my deepest gratitude to my supervisor Dr. Halil Ersin SÖKEN for his constant guidance, patience, encouragement and mentorship throughout the journey. I also would like to thank Prof. Dr. Ozan TEKİNALP for his support, suggestions and invaluable remarks.

I am grateful to my fellow colleagues in ROKETSAN for their support and friendship.

Last but not least, I am deeply indebted to my beloved family, mother Seven, father Murat and brother Ege Çetin. I always feel so lucky to have such a great family and would like to express my gratitude for their everlasting encouragement and patience throughout my life. Finally, I would like to thank to my lovely Sezin for her patience, support and love. This study wouldn't be possible without them.

This study is supported in part by the ERG project of ISAS/JAXA. We thank ERG project managers for allowing us to use the magnetometer data from the spacecraft to test our proposed algorithm.

TABLE OF CONTENTS

LIST OF TABLES

TABLES

LIST OF FIGURES

FIGURES

LIST OF ABBREVIATIONS

ERG	Exploration of energization and Radiation in Geospace also known as "ARASE"
DCM	Direction Cosine Matrix
ECEF	Earth Centered Earth Fixed Reference Frame
ECI	Earth Centered Inertial Reference Frame
EKF	Extended Kalman Filter
GAS	Geomagnetic Aspect Sensor
IAGA	International Association of Geomagnetism and Anomaly
IGRF	The International Geomagnetic Reference Field
ISAS	Institute of Space and Astronautical Science
KF	Kalman Filter
LEO	Low Earth Orbit
LS	Least Squares
NED	North-East-Down Reference Frame
TAM	Three-axis Magnetometer
UKF	Unscented Kalman Filter
JAXA	Japan Aerospace Exploration Agency

CHAPTER 1

INTRODUCTION

1.1 Motivation and Problem Definition

Attitude determination and control have vital role in aerospace applications. Spin stabilization is one of the simplest methods for stabilizing the attitude of a spacecraft and was widely employed since early era of space exploration [8]. Due to recent developments in technology, reduction of financial costs thanks to capability of multiple satellite orbital deployment with a single launch vehicle, the number of small satellites in the orbit has steeply increased [9]. As the number of micro and nano satellites increases, due to its simplicity use of spin stabilization gains trend and find a wide application field. Satellites could benefit from spin stabilization for their entire mission period or in some portion of the mission phase such as deorbiting of the spacecraft [10].

Three axis magnetometers (TAMs) are commonly used attitude sensors, not just for spacecraft but also for many other platforms from projectiles to unmanned aerial vehicles. They are practical, robust, lightweight and have low power consumption. For those reasons, most of small satellites and low Earth orbit (LEO) spacecraft have TAMs in their sensor package. Sensor measures magnetic field vector in vehicle's body frame and it is well known that attitude information can be extracted from TAMs when the measurements are combined with the inertial sensors [11] or a dynamic model in an estimation algorithm such as a Kalman filter (KF) [12]. Nonetheless accuracy of the estimation is limited with sensor errors, unless they are taken care of. Various solutions have been suggested to deal with these errors and appropriate calibration algorithm is mandatory for utilizable measurements. A comprehensive

literature survey about magnetometer errors and calibration algorithms, specifically for small satellite applications, is conducted by Soken [13].

There are various reasons behind the errors in magnetometer measurements. However, mathematically they could be boiled down to three branches; bias, scale-factor and misalignment errors. Inherently, errors may be reasoning from manufacturing and assembly processes as well as formed due to the spacecraft internal/external disturbances during the operational period. Corresponding errors can show constant or time-varying behaviors. For example, during eclipse period absorbed sun light from solar panel decreases so does the generated power and current profile inside the spacecraft. This profile change may result also change in electromagnetic interference and this phenomena brings even more problems for closely located avionics especially for small satellites. In such case, variations of magnetometer bias terms is very likely [14, 15]. Under those considerations, proposed calibration algorithm needs to be capable of estimating the varying errors.

In this thesis, an Unscented Kalman Filter (UKF) algorithm for real-time attitude-independent complete magnetometer calibration for spinning spacecraft and estimating all the error terms including; biases, scale-factors and misalignment terms is proposed. In a premise study [16], calibration was conducted with a pseudo-linear KF and by taking the advantage of the spinning spacecraft dynamics. The proposed algorithm estimates only the magnetometer bias errors. This study extends the scope, and with the help of proposed four quasi-measurements, which were derived using dynamic characteristics of spacecraft, ensures a complete calibration algorithm that is suitable to be implemented in real-time. In an earlier presented version [17] the algorithm was run using only three quasi-measurements. The proposed quasi-measurements considerably improve the convergence characteristics of the filter and the estimation accuracy compared to the UKF given in [18]. The algorithm is tested with both simulations and also with real magnetometer data from the Exploration of energization and Radiation in Geospace (ERG a.k.a ARASE) spacecraft of Japan Aerospace Exploration Agency (JAXA). The results are compared with those obtained using the TWO-STEP algorithm, the EKF and UKF given in [18].

1.2 Literature Survey

In literature, magnetometer calibration is carried out under two main approaches; batch and recursive algorithms. In batch calibration algorithms, magnetometer measurements are collected for some portion of the mission and then post-processed to estimate the sensor errors. Batch magnetometer calibration algorithms have an optimization process at the core and aim at minimizing the certain cost functions [19]. This approach could be repeated for many times during satellite mission period. A very common observation that can be used for such batch calibration algorithm is the magnitude difference for body frame magnetometer vector measurements and geomagnetic reference magnetic field vector. In ideal case, without any error, those two vectors have the same magnitude. In literature, TWO-STEP [20] by Alonso and Shuster is the most robust and well-known batch magnetometer calibration algorithm compared to other solutions. Alonso and Shuster developed the algorithm for bias errors only and then offered an extended version to cover the whole error space [21].

Although, batch algorithms with modified measurement models [15] can capture time-varying errors, due to the post-processing nature they cannot be executed in real-time and still does not respond to sudden unmodeled environmental changes. Thus, using real-time executable, recursive algorithms are important to meet mission requirements. Regarding this fact, Crassidis [18] proposed a real-time, attitude independent magnetometer calibration algorithm which is essentially using the same observation with TWO-STEP. However, due to highly non-linear measurement model the algorithm could perform successful results only when structured as an UKF but had divergence problems when structured as an extended Kalman filter (EKF).

Recent studies on magnetometer calibration propose attitude-independent real-time algorithms based on gyro or relative angular position measurements. In [22] a calibration algorithm based on online-nonlinear programming is proposed. Sakai et al. [23], Troni and Eustice [24] and Fedele et al. [25] used similar approaches to design Kalman filter algorithms for magnetometer calibration. It is assumed that the reference magnetic field does not change for successive measurements within a short sampling time. All these above mentioned studies estimate only the bias errors and assume that other magnetometer error terms are negligible. In [26] the authors again

build their algorithm based on the assumption that the Earth's magnetic field does not change within a short time in between two consecutive measurements. First a quasi-measurement is derived in the light of this assumption and then a sliding window filter, which is designed in the framework of an EKF, is used to estimate the magnetometer error terms. A complete calibration algorithm is proposed but no use of the spinning vehicle dynamics was made while designing the algorithm.

1.3 Contributions and Novelties

The contribution of the the thesis to the literature can be summarized as follows;

- Design of recursive magnetometer calibration algorithm which is capable of conducting real-time, attitude-independent, full state calibration.
- Performance of designed calibration algorithm is enhanced by use of additional measurements, named quasi measurements. Those measurements are not directly measured and instead derived using the dynamical characteristics and orbital properties of the aerospace vehicle.

1.4 The Outline of the Thesis

Chapter 1, is an overview to the thesis. Consists of problem definition and motivation, literature survey, contributions and the thesis outline.

Chapter 2, discusses the magnetometer measurement model in detail. Error model for the magnetometer is presented and a brief error model overview is conducted to visualize how each error term distorts the magnetometer measurements.

Chapter 3, presents the magnetometer calibration algorithms. Batch and recursive algorithms are studied in detail. Then the preferred, recursive algorithm's pros and cons are listed against batch approach.

Chapter 4, introduces three categories of quasi-measurements. The assumptions and motivations behind the derivations are explained. This chapter holds the main moti-

vation of the thesis.

Chapter 5, presents the application of the proposed algorithms with hypothetical and real satellite measurements. Results are discussed and compared.

Chapter 6, is for the finale, conclusion of the thesis. Future studies are discussed as well.

CHAPTER 2

MODELLING MAGNETOMETER MEASUREMENTS

Developing a test environment is one of the primary tasks for algorithm development. Because without a proper test environment performance evaluation, sensitivity, robustness and coverage analysis cannot be possible. In this chapter magnetometer sensor modelling is introduced. Modelled magnetometer data help to evaluate and compare the performance of the algorithms in upcoming chapters.

In Section 2.1, common magnetometer errors terms are presented and distortion effects over magnetometer measurements are discussed. Section 2.2, briefly explains Geomagnetic reference field model, Section 2.3, discusses the kinematic relations and transformation matrices, and finally, Section 2.4, uses error terms and reference magnetic field model to form magnetometer measurements.

2.1 Errors for Magnetometer

There could be numerous reasons behind the errors for magnetometer measurements [13]. Common error types for magnetometers are summarized in Fig. 2.1. Errors caused by internal or external disturbances are given with white background. Inherit sensor errors, from manufacturing or assembly, are illustrated with dark gray background. Finally, in the middle, errors that appear as a combination of both inheritance and disturbances are given with light gray background.

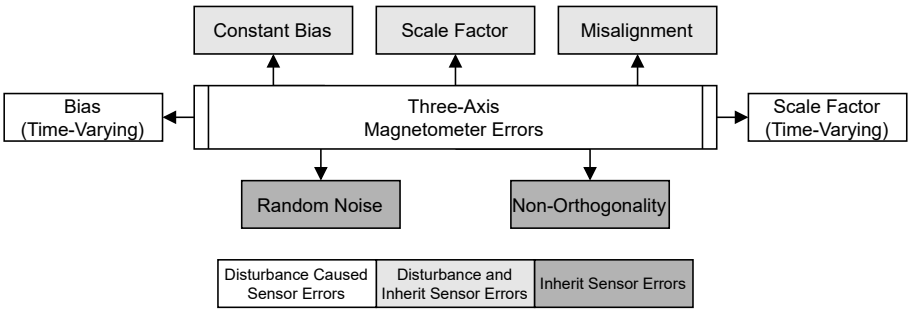

Figure 2.1: Magnetometer Errors Diagram

2.1.1 Soft-Iron Error

Externally applied magnetic field results in generation of magnetic field for soft-iron materials. Applied magnetic field's direction and magnitude directly affect the magnetic field generated by these materials. As result, soft-iron materials distort magnetometer measurements according to properties of the generated magnetic field. Measurements are distorted with a time-varying scale factor. Soft-iron errors can be represented with 3×3 matrix, D_{si}.

$$D_{si} = \begin{bmatrix} \beta_{xx} & \beta_{xy} & \beta_{xz} \\ \beta_{yx} & \beta_{yy} & \beta_{yz} \\ \beta_{zx} & \beta_{zy} & \beta_{zz} \end{bmatrix} \tag{2.1}$$

where soft-iron coefficients are given with β_{ij}. They create relation between the induced magnetic field generated by soft-iron material and the applied magnetic field.

D_{si} could be taken as a constant matrix [27]. This assumptions holds if magnetic field sources such as, actuators or high current flowing electrical wires are located reasonably far from magnetometers. For large spacecraft this solution is applicable. However, for small satellites all components need to be fitted in small volume therefore, error model should consider the time variation in the coefficients.

2.1.2 Hard-Iron & Null-Shift Error

Hard-iron errors are originated from permanent magnetic fields and impose bias on magnetometer measurements. Corresponding bias term, $\mathbf{b}_{hi}$ needs to be in-flight calibrated since it can change after the launch or varies with time [14]. However, hard-iron bias term could be assumed constant after spacecraft reaches its orbit.

Null-shift error, $\mathbf{b}_{ns}$, can occur due to sensor inheritance or manufacturing processes and imposes also constant bias on magnetometer measurements.

2.1.3 Time-varying Bias

Magnetic field profile inside the satellite is not constant due to constantly changing environmental conditions such as orbital position, expansion/collapsing due to solar exposure and power demand of the actuators. Considering the satellite variable conditions, direction and magnitude of the time-varying bias may become small or large compared to permanent hard-iron bias in 2.1.2. Therefore, it would be reasonable to collect all bias terms, 2.1.1 and 2.1.2, under single time-varying bias vector and perform in-flight calibration.

$$\mathbf{b} = \mathbf{b}_{si} + \mathbf{b}_{hi} + \mathbf{b}_{ns} \tag{2.2}$$

2.1.4 Scale Factor Error

Three axis magnetometer is comprised of orthogonally placed magnetometer triad. Without any error, measurement of three sensors should be equal when same input is given. However, in reality sensitivity of each magnetometer differs. To fix each magnetometer's output the corresponding measurement needs to be corrected with a sensitivity coefficient, named the scale factor.

Scale factor errors, D_{sf}, can be represented with a 3×3 matrix,

$$D_{sf} = \begin{bmatrix} 1+\xi_x & 0 & 0 \\ 0 & 1+\xi_y & 0 \\ 0 & 0 & 1+\xi_z \end{bmatrix} \tag{2.3}$$

where ξ_x, ξ_y and ξ_z are the scale factor coefficients.

2.1.5 Non-Orthogonality Error

Ideally, magnetometer triad has orthogonal placement for best coverage in Cartesian space. Improper placement of each magnetometer axis imposes reflection on the other axes. Non-orthogonality is represented with D_{no} matrix,

$$D_{no} = \begin{bmatrix} 1 & 0 & 0 \\ \sin\rho & \cos\rho & 0 \\ \sin\phi\cos\lambda & \sin\lambda & \cos\phi\cos\lambda \end{bmatrix} \tag{2.4}$$

where ρ, ϕ and λ are representing the angles between y sensor axis with y axis, z sensor axis with yz plane and z sensor axis with yz plane. Brief illustration is provided in Fig. 2.2

2.1.6 Misalignment Error

For perfect measurements, exact alignment of magnetometer sensor frame with respect to the spacecraft body frame is required. However, perfect alignment cannot be achieved in real applications. Therefore, residual of measurements dissolve across different axes due the difference in the desired sensor frame and actual sensor frame. Manufacturing processes or occurred due to vibrations in launch can cause misalignment errors. They can be represented by a skew-symmetric matrix, D_{ma}, formed by three small angles.

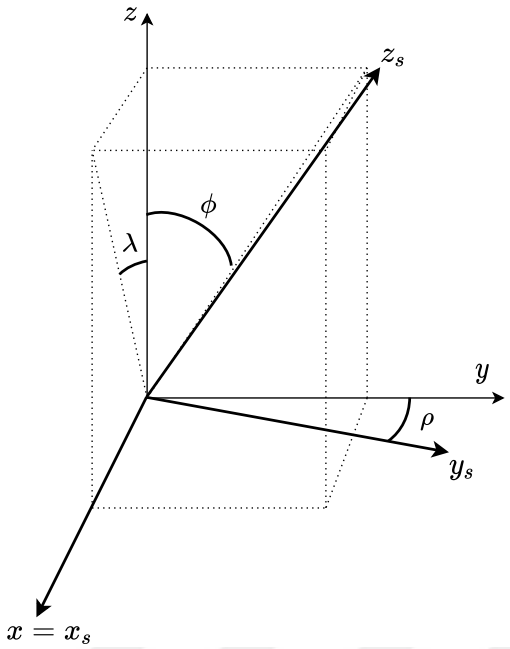

Figure 2.2: Non-Orthogonality Representation for Three-Axis Magnetometers

$$D_{ma} = \begin{bmatrix} 1 & -\varepsilon_z & \varepsilon_y \\ \varepsilon_z & 1 & -\varepsilon_x \\ -\varepsilon_y & \varepsilon_x & 1 \end{bmatrix} \tag{2.5}$$

2.2 International Geomagnetic Reference Field Model (IGRF)

The International Geomagnetic Reference Field (IGRF) is a standardized representation of the Earth's magnetic field and corresponding secular deviations. Magnetic field mathematical model derived by fitting parameters according to data collected from field surveys, observations and satellite measurements across the globe. International Association of Geomagnetism and Aeronomy (IAGA) [28] has been developed and still updating IGRF model since 1965.

The IGRF model updated in five year intervals. Therefore, relatively wide time-span have been covered with a single version. Most utilizable model outputs are available for the current time and for future dates model provides only a prediction. The current 13^{th} version of the IGRF model was published in December 2019 and covers from

years 1900 until 2025 [1].

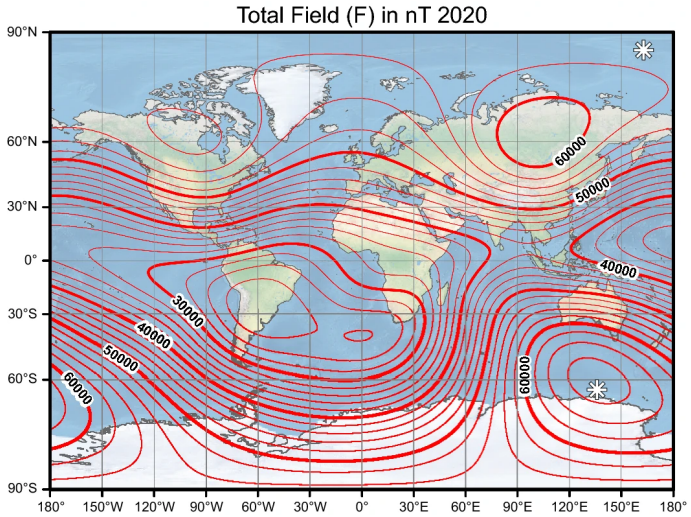

Figure 2.3: Map of Total Magnetic Field (2020) [1]

2.2.1 Spherical Harmonics

The IGRF model uses gradient of magnetic scalar potential, $V(r, \phi, \theta, t)$ to obtain geomagnetic field, $\vec{B}(r, \phi, \theta, t)$,

$$\vec{B}(r, \phi, \theta, t) = -\nabla V(r, \phi, \theta, t) = -\left(\frac{\partial V}{\partial r}, \frac{1}{r}\frac{\partial V}{\partial \theta}, \frac{1}{r \sin\theta}\frac{\partial V}{\partial \phi}\right) \tag{2.6}$$

The magnetic scalar potential model is represented by Gauss coefficients which one expressed using the spherical harmonic expansion of V,

$$\vec{B}(r, \phi, \theta, t) = a \sum_{l=1}^{L} \sum_{m=0}^{l} \left(\frac{a}{r}\right)^{l+1} \left(g_l^m(t) \cos m\phi + h_l^m(t) \sin m\phi\right) P_l^m \cos\theta \tag{2.7}$$

in which r is the distance from Earth's center, L is the degree of the expansion, ϕ is longitude, θ is co-latitude(the polar-angle), a is the Earth's radius, g_l^m and h_l^m correspond to Gauss coefficients, and $P_l^m \cos\theta$ are the Schmidt normalized Legendre functions of degree l and order m,

$$P_n^m \cos\theta = (-1)^m (\sin\theta)^{m/2} \frac{d^m}{d(\cos\theta)^m} P_n \cos\theta \tag{2.8}$$

which,

$$P_n \cos\theta = \frac{1}{2^n n!} \left[\frac{d^n}{d(\cos\theta)^n} \left((\cos\theta)^2 - 1 \right)^n \right] \tag{2.9}$$

This model assuming Gauss coefficients are prone to change linearly over the corresponding time interval.

By using the IGRF model, magnetic field vector is obtained in NED (North-East-Down Local Level Reference Frame). To perform calibration, NED resolved magnetic field vector need to presented in spacecraft body frame. Required attitude representation methods, defined reference frame and associated transformation matrices are presented in section 2.3.

2.3 Attitude Representations & Reference Frames

The purpose of this section is to give the reader insight for attitude representations, reference frames and transformation matrices. The information provided here will be used to transport IGRF magnetometer model output in NED frame to spacecraft body frame where the magnetometer is located.

2.3.1 Attitude Representations

Orientation relation between two reference frame is expressed with the attitude information. Since we are interested in the attitude of the satellite with respect to a selected reference frame, in our case orbital and the satellite body frame. There are various methods available to express attitude such as DCM (Direction Cosine Matrix), Euler Angles.

2.3.1.1 Direction Cosine Matrix (DCM)

First we need to define a reference frame α, which represented with $\{\vec{i}, \vec{j}, \vec{k}\}$ orthogonal unit vectors. For the other reference frame, β, which has orthogonal unit vectors of $\{\vec{u}, \vec{v}, \vec{w}\}$. In order to express representation of a vector in terms of $\{\vec{i}, \vec{j}, \vec{k}\}$ with $\{\vec{u}, \vec{v}, \vec{w}\}$, we need to perform following operation,

$$\begin{bmatrix} \vec{u} \\ \vec{v} \\ \vec{w} \end{bmatrix} = \begin{bmatrix} \vec{u} \\ \vec{v} \\ \vec{w} \end{bmatrix} \begin{bmatrix} \vec{i} & \vec{j} & \vec{k} \end{bmatrix} \begin{bmatrix} \vec{i} \\ \vec{j} \\ \vec{k} \end{bmatrix} \tag{2.10a}$$

$$\begin{bmatrix} \vec{u} \\ \vec{v} \\ \vec{w} \end{bmatrix} = \underbrace{\begin{bmatrix} \vec{u}\vec{i} & \vec{u}\vec{j} & \vec{u}\vec{k} \\ \vec{v}\vec{i} & \vec{v}\vec{j} & \vec{v}\vec{k} \\ \vec{w}\vec{i} & \vec{w}\vec{j} & \vec{w}\vec{k} \end{bmatrix}}_{C} \begin{bmatrix} \vec{i} \\ \vec{j} \\ \vec{k} \end{bmatrix} \tag{2.10b}$$

where $\vec{u}\vec{i} = |\vec{u}| \cdot |\vec{i}| \cos\theta$ and C corresponds to DCM. $\{\vec{i}, \vec{j}, \vec{k}\}$ and $\{\vec{u}, \vec{v}, \vec{w}\}$ are unit vectors and their norm product equals to 1. Therefore, each element of the DCM matrix gives the related cosine angle between corresponding vectors. Equation 2.10b can be written as,

$$\begin{bmatrix} \vec{u} \\ \vec{v} \\ \vec{w} \end{bmatrix} = \begin{bmatrix} C_{11} & C_{12} & C_{13} \\ C_{21} & C_{22} & C_{23} \\ C_{31} & C_{32} & C_{33} \end{bmatrix} \begin{bmatrix} \vec{i} \\ \vec{j} \\ \vec{k} \end{bmatrix} = C_{\beta\alpha} \begin{bmatrix} \vec{i} \\ \vec{j} \\ \vec{k} \end{bmatrix} \tag{2.11}$$

In the literature, $C_{\beta\alpha}$ can also be named as coordinate transformation matrix or rotation matrix. It is an orthogonal matrix which means, its inverse equals to its transpose.

$$C_{\beta\alpha}^{-1} = C_{\beta\alpha}^{T} \tag{2.12}$$

2.3.1.2 Euler Angles

To transform a vector from one frame to another frame coordinate transformation matrix is required. In order to define such orientation uniquely, Euler angles are proposed. Those angles aare defined for successive rotation of intermediate frames. Three angles are used to express unique orientation and 12 sets of rotation sequence can be used.

Recall the rotation matrix in Equation 2.11, $C_{\beta\alpha}$, Three rotations are required to transform vector from frame α to β. For that rotation 3-2-1 sequence is used. The rotation starts from z axis and follows up with y and x axis. Rotation sequence is given below where (ξ) and variants denote the intermediate frames and $[\gamma_1\,\gamma_2\,\gamma_3]$ are corresponding Euler Angles.

$$C_3(\gamma_3) : \alpha \longrightarrow \xi \tag{2.13a}$$

$$C_2(\gamma_2) : \xi \longrightarrow \xi' \tag{2.13b}$$

$$C_1(\gamma_1) : \xi' \longrightarrow \beta \tag{2.13c}$$

Expanding the relation, which is given in Equation 2.13,

$$\begin{bmatrix}\vec{\xi_1}\\ \vec{\xi_2}\\ \vec{\xi_3}\end{bmatrix} = \begin{bmatrix}\cos\gamma_3 & \sin\gamma_2 & 0\\ -\sin\gamma_3 & \cos\gamma_3 & 0\\ 0 & 0 & 1\end{bmatrix}\begin{bmatrix}\vec{i}\\ \vec{j}\\ \vec{k}\end{bmatrix} = C_3(\gamma_3)\begin{bmatrix}\vec{i}\\ \vec{j}\\ \vec{k}\end{bmatrix} \tag{2.14a}$$

$$\begin{bmatrix}\vec{\xi_1}'\\ \vec{\xi_2}'\\ \vec{\xi_3}'\end{bmatrix} = \begin{bmatrix}\cos\gamma_2 & 0 & -\sin\gamma_2\\ 0 & 1 & 0\\ \sin\gamma_2 & 0 & \cos\gamma_2\end{bmatrix}\begin{bmatrix}\vec{\xi_1}\\ \vec{\xi_2}\\ \vec{\xi_3}\end{bmatrix} = C_2(\gamma_2)\begin{bmatrix}\vec{\xi_1}\\ \vec{\xi_2}\\ \vec{\xi_3}\end{bmatrix} \tag{2.14b}$$

$$\begin{bmatrix}\vec{u}\\ \vec{v}\\ \vec{w}\end{bmatrix} = \begin{bmatrix}1 & 0 & 0\\ 0 & \cos\gamma_1 & -\sin\gamma_1\\ 0 & \sin\gamma_1 & \cos\gamma_1\end{bmatrix}\begin{bmatrix}\vec{\xi_1}'\\ \vec{\xi_2}'\\ \vec{\xi_3}'\end{bmatrix} = C_1(\gamma_1)\begin{bmatrix}\vec{\xi_1}'\\ \vec{\xi_2}'\\ \vec{\xi_3}'\end{bmatrix} \tag{2.14c}$$

Using Euler Angles for attitude representation is easier with smaller dimensions compared to DCM. However, singularity problem limits their application in practice. Also

trigonometric functions are not linear with Euler angles [29].

2.3.2 Reference Frames

Reference frames as name suggest serves as a reference to express the position and attitude of a body with respect to corresponding reference. Reference frames that have been used in this thesis are discussed in this section.

2.3.2.1 Earth Centered Inertial Reference Frame - ECI

Earth Centered Inertial (ECI) has origin at the center of the Earth and orientation is fixed with respect to stars. In other words, it is not rotating. Newton's law are only applicable in inertial frames. Also, inertial sensors perform measurements with respect to inertial frames. For near Earth applications the Earth centered inertial frame can be used as reference frame. Axes ECI frame are presented in Figure 2.4 where X_i, Y_i and Z_i denotes the axes.

- The Z_i axis is showing the geographic North Pole.
- The X_i axis towards Vernal equinox (γ) which is the point where the Sun crosses the celestial Equator in March on its way from South to North.
- The Y_i formed according to keep right hand rule as the cross product of Z_i and X_i axes.

2.3.2.2 Earth Centered Earth Fixed Reference Frame - ECEF

An Earth Centered Earth fixed Reference Frame known as Earth frame, is similar to ECI except that all axes are fixed with Earth. Both reference frames share the same center, modelled center of the ellipsoid.

- The Z axis is the same with the ECI fram and pointing towards true North Pole.

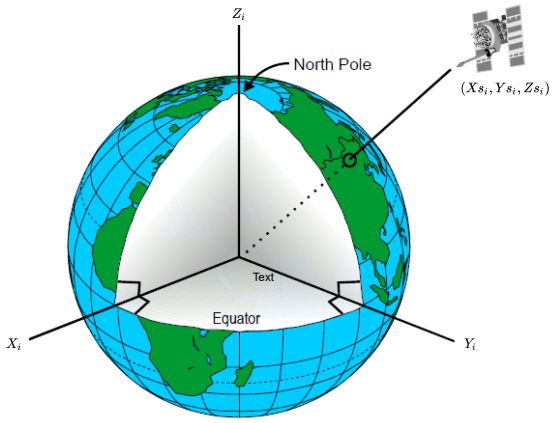

Figure 2.4: Earth Centered Inertial Frame [2]

- The X axis is pointing towards the intersection of Equator and the Reference Meridian in other words zero-meridian which defines the $0°$ longitude, λ_b.
- Finally, Y axis, completes the right handed orthogonal set.

2.3.2.3 Local Level Reference Frame - NED

The local navigation frame known as local level frame. Its origin is described by the navigation solution. Origin could be part of the navigation system or coincident with the center of mass of the the object. Axes are aligned with the topographic directions.

- Z axis known as the D (Down) is defined as the normal to the ellipsoid surface.
- X axis is in the orthogonal plane to the Z axis and to pointing to line from origin to the north pole.
- Finally, Y axis, completes the right handed orthogonal set.

2.3.2.4 Orbital Reference Frame

Orbital reference frame moves with the spacecraft during the orbital period. Especially for nadir-pointing satellites, orbital frame can be used as reference to represent attitude of the spacecraft. We usually, define satellite's motion in ECI but attitude

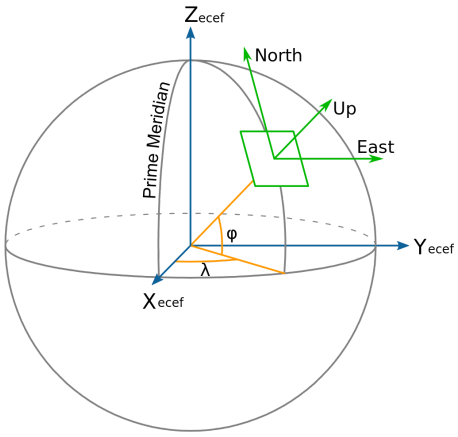

Figure 2.5: Origin and axes of NED and ECEF Frame [3]

might be shown with respect to orbital frame. Like body reference frame, (Section 2.3.2.5), origin of the frame located on center of mass of the spacecraft. As given in Figure 2.6.

- The Z_o is the nadir direction (pointing towards center of Earth).
- The Y_o is tangential to orbit which can be aligned with spacecraft velocity vector in case of circular orbit
- The X_o forms the orthogonal right hand rule.

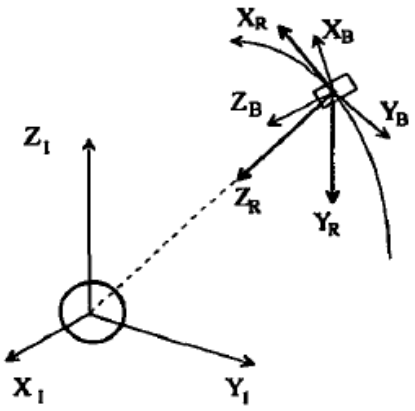

Figure 2.6: Orbital Reference Frame [4]

2.3.2.5 Spacecraft Body Reference Frame

The spacecraft body frame is an vehicle carried reference frame which means it is moving and rotating with spacecraft body. Origin of the frame is located on center of mass of the spacecraft. Inertial sensor (accelerometers, gyroscopes, magnetometers, etc.) are mounted as to be aligned with this frame. Therefore, measurements are resolved in this frame. Three parameters named as Euler angles set the condition of body frame related to the reference coordinate system. The main purpose of the attitude estimation and control is to estimate and control the orientation of this body frame relative to the external reference frame.

Axes Body frame are presented in Figure 2.7 where X_b, Y_b and Z_b denotes the axes.

- The X_b axis is the roll axis
- The Y_b is the pitch axis
- Finally, Z_b is the yaw axis, formed according to keep right hand rule as the cross product of X_b and Y_b axes.

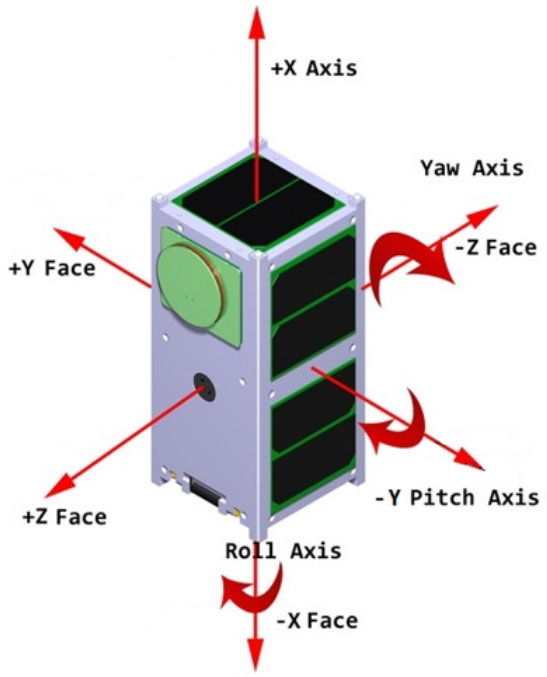

Figure 2.7: Earth Centered Inertial Frame [5]

2.3.3 Reference Frame Transformations

To find representation of a vector in another reference frame, production with an DCM matrix is required. Rotation matrix is expressed with C_{α}^{β} where subscript, α, denotes the origination frame and superscript, β, denotes the target frame.

2.3.3.1 ECEF to ECI

The center and the Z axis of ECEF and ECI frame are coincident. The major difference between them is, ECEF is rotating with Earth while orientation of ECI is fixed respect to stars. Although, X and Y axes become coincident at time $t = t_0$ and the reference frame ECEF rotates about Z axis at $\omega_{ie} \simeq 7.292115 \times 10^{-5}\, rad/s$.

$$C_e^i = \begin{bmatrix} \cos\omega_{ie}(t-t_0) & -\sin\omega_{ie}(t-t_0) & 0 \\ \sin\omega_{ie}(t-t_0) & \cos\omega_{ie}(t-t_0) & 0 \\ 0 & 0 & 1 \end{bmatrix} \tag{2.15}$$

2.3.3.2 NED to ECEF

Relative orientation relation between Earth and local level frames is expressed by the geodetic latitude, L_b, and longitude, λ_b, of the body frame whose center is coincident with local navigation frame.

$$C_n^e = \begin{bmatrix} -\sin L_b \cos\lambda_b & -\sin\lambda_b & -\cos L_b \cos\lambda_b \\ -\sin L_b \sin\lambda_b & \cos\lambda_b & -\cos L_b \sin\lambda_b \\ \cos L_b & 0 & -\sin L_b \end{bmatrix} \tag{2.16}$$

2.3.3.3 Orbital Frame to ECI

The rotation from orbital frame to ECI frame is derived from position vector, $\vec{r}_i$, and velocity vector, $\vec{v}_i$ of the spacecraft in ECI frame,

$$\vec{o}_3 = -\frac{\vec{r}_i}{\|\vec{r}_i\|} \tag{2.17a}$$

$$\vec{o}_2 = \frac{\vec{r}_i \times \vec{v}_i}{\|\vec{r}_i \times \vec{v}_i\|} \tag{2.17b}$$

$$\vec{o}_1 = \vec{o}_2 \times \vec{o}_3 \tag{2.17c}$$

$$C_o^i = \begin{bmatrix} \vec{o}_1 & \vec{o}_2 & \vec{o}_3 \end{bmatrix}_{3\times 3} \tag{2.17d}$$

2.3.3.4 Orbital Frame to Body Frame

The rotation from orbital frame to body frame. Rotation matrix formed by using three consecutive rotations respectively by attitude angles; yaw (ψ), pitch (θ) and roll (ϕ),

$$C_o^b = \begin{bmatrix} 1 & 0 & 0 \\ 0 & \cos\phi & \sin\phi \\ 0 & -\sin\phi & \cos\phi \end{bmatrix} \begin{bmatrix} \cos\theta & 0 & -\sin\theta \\ 0 & 1 & 0 \\ \sin\theta & 0 & \cos\theta \end{bmatrix} \begin{bmatrix} \cos\psi & \sin\psi & 0 \\ -\sin\psi & \cos\psi & 0 \\ 0 & 0 & 1 \end{bmatrix} \tag{2.18}$$

2.4 Magnetometer Measurement Model

This section serves as a conclusion for this chapter. Main objective is combining magnetometer errors in Section 2.1 with reference magnetic field model, IGRF, in section 2.2 by using the proposed relations given in Section 2.3.

Although, different source of magnetometer errors explained in detail, their individual effect over magnetometer measurements cannot be distinguished mathematically. Therefore, they could be boiled down to three main categories; bias, scale-factor and misalignment errors [20]. Generic magnetometer model can be represented as,

$$\mathbf{B_k} = (I_{3\times 3} + D_k)^{-1}(A_k\mathbf{H_k} + \mathbf{b_k} + \epsilon_\mathbf{k}), \quad k = 1, 2, ...N \tag{2.19}$$

where $\mathbf{B_k}$ is the magnetometer measurement vector, $\mathbf{H_k}$ is the reference magnetic field measurement resolved in inertial frame and D is the scaling matrix, formed

by combination of scale factor, non-orthogonality and misalignment error terms. $\mathbf{b_k}$ represents the bias vector and $\epsilon_\mathbf{k}$ is the measurement noise vector that is assumed to be zero-mean Gaussian with covariance Σ_k as $\epsilon_\mathbf{k} \sim N(0, \Sigma_k)$. A_k is the attitude matrix, which represents attitude of the spacecraft body frame with respect to the inertial frame.

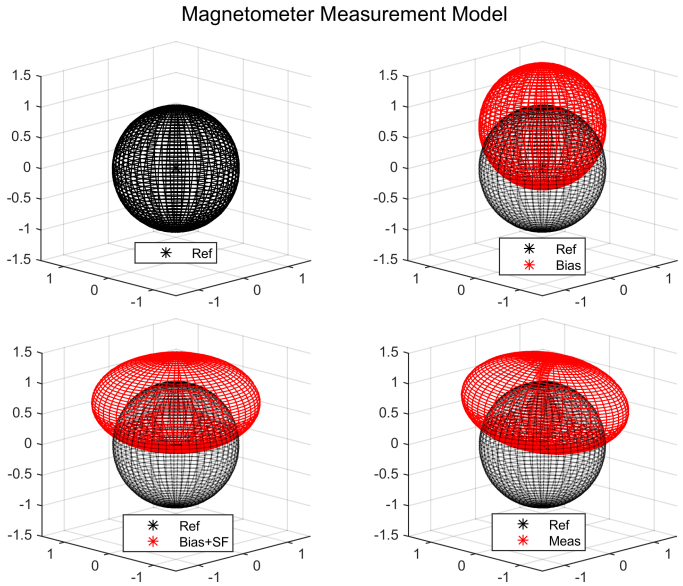

Figure 2.8: Effect of Magnetometer Errors on Measurements

Magnitude of the perfect magnetometer measurement does not change with the orientation of the sensor frame. Measurements collected by rotating the sensor frame in different orientations forms a perfect sphere. All bias related terms in equation 2.19, shift the sphere locus. Diagonal terms on scaling matrix, D, change sphere into an ellipsoid. Off-diagonal terms of D, skew and change rotation of the ellipsoid. All these effects are illustrated in Fig. 2.8 respectively.

CHAPTER 3

MAGNETOMETER CALIBRATION ALGORITHMS

This chapter aims explaining full state calibration algorithms which have been used in this thesis, well known batch method, TWO-STEP [20], and real-time, recursive method conducted with EKF and UKF [18]. These algorithms serve as benchmark to evaluate and compare the performance of proposed the calibration algorithm.

This chapter has two main sections; Section 3.1 starts with brief overview about batch calibration algorithms. Then the corresponding cost function is presented and the section is concluded with TWO-STEP algorithm. Section 3.2, starts with an overview for recursive calibration algorithms and continues with derivation of the attitude independent measurement. Section concluded with the EKF and UKF algorithms.

3.1 Batch Calibration Algorithms

3.1.1 Overview

Batch calibration algorithms, as name suggests, process batch of data for estimating the calibration parameters. Corresponding data could belong to some portion of the mission period. We should keep in mind that, the estimation accuracy is related to stored data. Batch methods have optimization algorithms at the core (Figure 3.1) and aims minimizing certain cost function (sec. 3.1.2).

Coverage for the estimations is related with selected measurement model. In [20] algorithm is proposed just for bias estimates then in the upcoming study [21] algorithm coverage is extended for scale-factor and misalignment error terms. Due to its nature, batch calibration algorithms are having struggle to deal with time-varying errors. One

Figure 3.1: Batch Calibration Algorithms' Illustration [6]

straightforward solution for time-varying errors is re-initializing batch calibration algorithm multiple times during the mission period. However, single estimate of error terms is provided after processing the measurements of the related period.

3.1.2 Cost Function

The origination point of batch magnetometer calibration algorithms come from an attitude-independent observation based on the fact that magnitudes of reference magnetic field vector and magnetometer measurement vector are same.

$$\mathbf{Z}_k = \|\mathbf{B}_k\|^2 - \|\mathbf{H}_k\|^2 = f(\mathbf{B}_k, \mathbf{X}) + \epsilon_{\mathbf{k}} \tag{3.1}$$

where $\mathbf{X}$ is the magnetometer error coefficients. $\epsilon_{\mathbf{k}}$ corresponds to measurement noise which can be approximated as Gaussian, $\epsilon_{\mathbf{k}} \sim N(\mu_k, \sigma_k^2)$. Here, mean denoted by μ_k, variance denoted by σ_k^2 and $E\{\}$ denotes the expectation, Gaussian process with covariance given by Σ_k.

$$\begin{aligned} \mu_k &= E\{\epsilon_{\mathbf{k}}\} = -\text{tr}(\Sigma_k) \\ \sigma_k^2 &= E\{\epsilon_{\mathbf{k}}^{\mathbf{2}}\} - \mu_k^2 \end{aligned} \tag{3.2}$$

Estimation accuracy of the error coefficients are related to finding global-minima of the cost function with the maximum likelihood criteria,

$$J(\mathbf{X}) = \frac{1}{2}\sum_{k=1}^{N}\left[\frac{1}{\sigma_k^2}\left(\mathbf{Z}_k - f(\mathbf{B}_k, \mathbf{X}) - \mu_k\right)^2 + \log\sigma_k^2 + \log 2\pi\right] \tag{3.3}$$

3.1.3 TWO-STEP Algorithm

There are various solutions available to minimize eq. 3.3 and find estimate for the error terms [13]. Nonetheless, Using TWO-STEP method is beneficial, since algorithm could converge even if others are struggling with divergence problems [18]. Furthermore, Alonso and Shuster elevated the coverage of preliminary algorithm [20] and enables estimation of scale-factor and non-orthogonality terms beside bias estimates [21].

Even the cost function for simple bias determination problem has quartic structure. Applying centering method is well known way to cope with such problem [30]. That would yields a quadratic cost function that can be minimized with Least-Squares(LS).

Addition of new step after centering approximation makes the difference. Centered estimate is used to initialize the iterative Newton-Gauss algorithm. This intuition gives the characteristic name, TWO-STEP, to the algorithm. To conclude, first centering is applied over measurements to get rough estimates, then that estimates employ LS to solve for global-minima.

Minimizing equation 3.3 is not straightforward due to negative-log-likehood function is quartic which results in multiple minima and maxima. Seeking for global minimum with initial conditions of null states does not guarantee for convergence as seen in [29]. Therefore, we need such a proper initial estimate, which can be provided by centering approximation.

The main goal is finding D and $\mathbf{b}$ in equation 2.19, we first need to start with defining quantities E and $\mathbf{c}$ in order to collect nonlinear dependency under single term.

$$E = 2D + D^2 \tag{3.4a}$$

$$\mathbf{c} = (I_3 + D)\mathbf{b} \tag{3.4b}$$

Where E is symmetric but not diagonal. Thus,

$$Z_k = -\mathbf{B}_k^T E \mathbf{B}_k + \mathbf{B}_k^T \mathbf{c} - |\mathbf{b}(c, E)|^2 + \nu_k \tag{3.5}$$

We could write,

$$\mathbf{B}_k^T E \mathbf{B}_k = \mathbf{K}_k \mathbf{E} \tag{3.6}$$

which,

$$\mathbf{K}_k = \begin{bmatrix} B_{1,k}^2 & B_{2,k}^2 & B_{3,k}^2 & 2B_{1,k}B_{2,k} & 2B_{1,k}B_{3,k} & 2B_{2,k}B_{3,k} \end{bmatrix} \tag{3.7a}$$

$$\mathbf{E} = \begin{bmatrix} E_{11} & E_{22} & E_{33} & E_{12} & E_{13} & E_{23} \end{bmatrix}^T \tag{3.7b}$$

Rearranging equation 3.5,

$$Z_k = -\mathbf{K}_k \mathbf{E} + 2\mathbf{B}_k^T \mathbf{c} - |\mathbf{b}(c, E)|^2 + \nu_k \tag{3.8a}$$

$$= \mathbf{L}_k \theta' - |\mathbf{b}(\theta')|^2 + \nu_k \tag{3.8b}$$

where,

$$\mathbf{L}_k \equiv \begin{bmatrix} \mathbf{B}_k^T & -\mathbf{K}_k \end{bmatrix} \tag{3.9a}$$

$$\theta' \equiv \begin{bmatrix} \mathbf{c} & \mathbf{E} \end{bmatrix}^T \tag{3.9b}$$

Here, θ' is a 9×1 and $\mathbf{L}_k$ is 1×9 matrices. Defining,

$$\bar{\mathbf{L}} \equiv \bar{\sigma}^2 \sum_{k=1}^{N} \frac{1}{\sigma_k^2} \mathbf{L}_k \tag{3.10a}$$

$$\tilde{\mathbf{L}}_k \equiv \mathbf{L}_k - \bar{\mathbf{L}} \tag{3.10b}$$

For centered and centered measurements,

$$\tilde{Z}_k = \tilde{\mathbf{L}}_k \cdot \theta' + \tilde{\nu}_k \tag{3.11a}$$

$$\bar{Z} = \bar{\mathbf{L}}\theta' - |\mathbf{b}(\theta')|^2 + \bar{\nu} \tag{3.11b}$$

Since D is no longer a diagonal matrix, we don't have a straightforward relation for $|\mathbf{b}(\theta')|^2$, which becomes,

$$|\mathbf{b}(\theta')|^2 = \mathbf{c}^T (I + D)^{-2} \mathbf{c} = \mathbf{c}^T (I + E)^{-1} \mathbf{c} \tag{3.12}$$

To obtain a system matrix, we need to take partial derivative of $|\mathbf{b}(\theta')|^2$,

$$\frac{\partial}{\partial \mathbf{c}_i} |\mathbf{b}(\theta')|^2 = 2((I_3 + E)^{-1}\mathbf{c})_i \tag{3.13a}$$

$$\frac{\partial}{\partial \mathbf{E}_{i,j}} |\mathbf{b}(\theta')|^2 = -(2 - \delta_{i,j})((I_3 + E)^{-1}\mathbf{c})_i((I_3 + E)^{-1}\mathbf{c})_j \tag{3.13b}$$

Here, $((I_3 + E)^{-1}\mathbf{c})_i$ is the i^{th} element of $((I_3 + E)^{-1}\mathbf{c})$. Furthermore, $\delta_{i,j}$ is the Kronecker delta function.

Again, we've used new quantities to collect nonlinear terms under $|\mathbf{b}(\theta')|^2$. At this point we will only need an initial condition to start with Which is derived using the centering approximation,

$$\tilde{\theta'}^* = \sum_{k=1}^{N} \frac{1}{\sigma_k^2} (\tilde{z}_k - \tilde{\mu}_k) \tilde{\mathbf{L}}_k^T \tag{3.14a}$$

$$= \sum_{k=1}^{N} \frac{1}{\sigma_k^2} \tilde{\mathbf{L}}_k \tilde{\mathbf{L}}_k^T \tag{3.14b}$$

With specified initial conditions iterations could start,

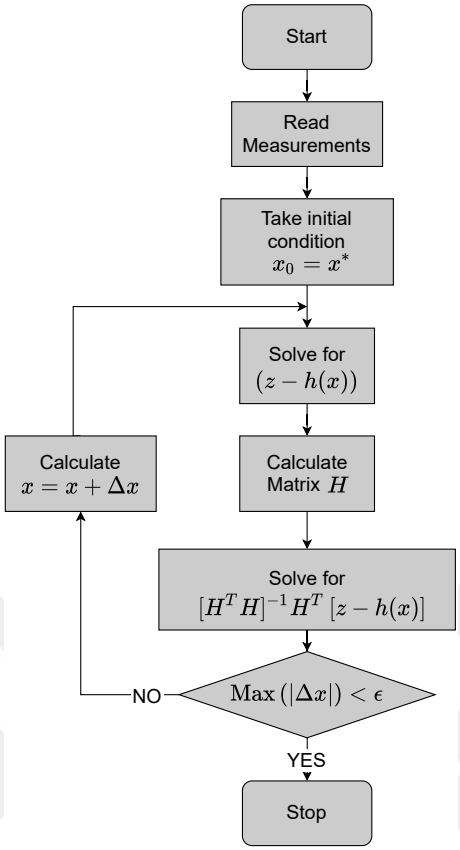

Figure 3.2: Least Squares Algorithm Flow Chart

To compute D^* and $\mathbf{b}^*$ from $\mathbf{E}^*$ and $\mathbf{c}^*$, we write,

$$\mathbf{E}^* = USU^T \tag{3.15}$$

Here S is diagonal and U is orthogonal,

$$S = \text{diag}(s_1, s_2, s_3) \tag{3.16}$$

Where we've defined W to be a diagonal matrix which satisfies,

$$S = 2W + W^2 \tag{3.17}$$

Diagonal elements of W have solution,

$$w_i = -1 + \sqrt{1 + si} \qquad i = 1, 2, 3 \tag{3.18}$$

The maximum likelihood estimation of scaling matrix which consists of scale factor and non-orthogonality is found as,

$$D^* = UWU^T \tag{3.19}$$

where again U is orthogonal matrix and finally maximum likelihood estimate of bias vector found as,

$$\mathbf{b}^* = (I_3 + D^*)^{-1}\mathbf{c}^* \tag{3.20}$$

3.2 Recursive Calibration Algorithms

3.2.1 Overview

Performing autonomous, real-time magnetometer calibration is in one of the common mission requirements for modern spacecrafts. TWO-STEP algorithm requires to iterate over same batch of data to present estimates. Therefore, cannot be used to perform real-time calibration. Recursive calibration algorithms perform magnetometer calibration in real-time. Common structure consists of two parts; system model and measurement update. In this thesis, magnetometer error terms modelled as they don't have dynamics and remain constant,

$$\dot{\mathbf{X}} = 0 \tag{3.21}$$

Recursive algorithms can deal with time-varying errors even with a really simple system model as given in eq. 3.21. This is one of the main advantage of recursive structure compared to batch algorithms. Unlike Batch algorithms, even general magnetometer measurement model eq. 2.19 would be sufficient and no additional terms are required.

The major challenge behind recursive algorithms is ensuring observability conditions. Algorithms require sufficient number of measurements to assure convergence to actual states.

3.2.2 Attitude-Independent Measurement

For building an attitude-independent observation, we use the fact that the magnitude of the magnetic field norm must be same in reference and spacecraft body frames for an ideal case. Derivation starts with eliminating attitude dependency in eq. 2.19 by simply transposing the terms and taking square. In the end we have the measurement as [18].

$$z_{1,k} = \|\mathbf{B_k}\|^2 - \|\mathbf{H_k}\|^2 \tag{3.22}$$

The measurement model is given by $z_k = h_k(x_k) + v_k$, where

$$h_{1,k}(x_k) = -\mathbf{B_k^T}(2D_k + D_k^2)\mathbf{B_k} + 2\mathbf{B_k^T}(I_{3\times3} + D_k)\mathbf{b_k} - \|\mathbf{b_k}\|^2 \tag{3.23}$$

The effective measurement noise v_k for this measurement is given by

$$v_k = 2[(I_{3\times3} + D_k)\mathbf{B_k} - \mathbf{b_k}]^T\epsilon_k - \|\epsilon_\mathbf{k}\|^2 \tag{3.24}$$

and it is approximately Gaussian with mean μ_k and variance σ_k^2 given as

$$\mu_k = -tr(\Sigma_k) \tag{3.25a}$$

$$\sigma_k^2 = 4\left[(I_{3\times3} + D_k)\mathbf{B_k} - \mathbf{b_k}\right]^T\Sigma_k\left[(I_{3\times3} + D_k)\mathbf{B_k} - \mathbf{b_k}\right] + 2(tr\Sigma_k^2) \tag{3.25b}$$

This is the first measurement to be used in the magnetometer calibration. Crassidis et al. [18] used only this measurement for designing different Kalman filtering algorithms. In this thesis, we refer to the UKF algorithm which is using only this measurement as the UKF with one measurement (1M).

3.2.3 Extended Kalman Filter Algorithm

In standard Kalman Filter, system and measurement model assumed to be linear. However, this assumption is hard to meet with most of the applications. A nonlinear form of the Kalman Filter is the extended Kalman Filter. In EKF, The nonlinear functions of, system model, $f(x)$ and measurement model, $h(x)$, are replaced with linearized forms, $F(x)$ and $H(x)$ respectively.

EKF is used to determine calibration parameters in real-time . An advantage of EKF is unlike centered approach given in Section 3.1.3 no need for conversion of states from b and D to c and E, respectively. The measurement model is given by $Z_k = h_k(x_k) + \upsilon_k$ which presented in eq. 3.23.

State vector consists of 3 bias, 3 scale-factor and 3 misalignment states and given in eq. 3.26

$$X = \begin{bmatrix} b_x & b_y & b_z & D_{11} & D_{22} & D_{33} & D_{12} & D_{13} & D_{23} \end{bmatrix}^T \tag{3.26}$$

Since system model is simple, $\dot{X} = 0$. Therefore, state and covariance propagation are rather straightforward. The relations for the measurement update are given as,

$$\hat{x}_{k+1} = \hat{x}_k + K_k \left[Z_k - h_k(\hat{x}_k) \right] \tag{3.27a}$$

$$P_{k+1} = \left[I_{9\times 9} - K_k H_k(\hat{x}_k) \right] P_k \tag{3.27b}$$

$$K_k = P_k H_k^T(\hat{x}_k) \left[H_k(\hat{x}_k) P_k H_k^T + R \right]^{-1} \tag{3.27c}$$

Here, P is the covariance of the estimated parameters for b and D. The 1×9 matrix $H(x)$ is the measurement matrix retrieved from the partial derivative of measurement function $h(x)$ respect to x.

$$H_1(x) = \begin{bmatrix} 2\mathbf{B}^T(I_{3\times 3} + D) - 2\mathbf{b}^T & -\mathbf{S}\frac{\partial E}{\partial D} + 2\mathbf{J} \end{bmatrix} \tag{3.28}$$

Relations for the $\mathbf{S}$, $\frac{\partial E}{\partial D}$ and $\mathbf{J}$ are given in eq. 3.29 and belong to same time step k,

$$\mathbf{S} = \begin{bmatrix} B_1^2 & B_2^2 & B_3^2 & 2B_1B_2 & 2B_1B_3 & 2B_2B_3 \end{bmatrix} \tag{3.29a}$$

$$\mathbf{J} = \begin{bmatrix} B_1b_1 & B_2b_2 & B_3b_3 & B_1b_2 + B_2b_1 & B_1b_3 + B_3b_1 & B_2b_3 + B_3b_2 \end{bmatrix} \tag{3.29b}$$

$$\frac{\partial E}{\partial D} = \begin{bmatrix} 2(1+D_{11}) & 0 & 0 & 2D_{12} & 2D_{13} & 0 \\ 0 & 2(1+D_{22}) & 0 & 2D_{12} & 0 & 2D_{23} \\ 0 & 0 & 2(1+D_{33}) & 0 & 2D_{13} & 2D_{23} \\ D_{12} & D_{12} & 0 & 2+D_{11}+D_{22} & D_{23} & D_{13} \\ D_{13} & 0 & D_{13} & D_{23} & 2+D_{11}+D_{33} & D_{12} \\ 0 & D_{23} & D_{23} & D_{13} & D_{12} & 2+D_{22}+D_{33} \end{bmatrix} \tag{3.29c}$$

3.2.4 Unscented Kalman Filter Algorithm

This section aims deriving the formulation for recursive unscented Kalman Filter Algorithm which is an alternative to EKF proposed in [31] named UKF. The idea behind the theory is, it would be easier to estimate Gaussian distribution compared to any arbitrary nonlinear function.

Propagation scheme of the UKF is different than the EKF. Having an $n \times n$ matrix P, a set of n points are generated using column of the matrix $\pm\sqrt{nP}$. The set of points has zero mean($\mu = 0$), but if has mean different than zero then simply adding corresponding mean to each point which brings symmetric $2n$ points with desired mean and covariance. Odd central moments equal to zero due to symmetricity of the set. Furthermore, its first three moment is equal to Gaussian distribution. More information is provided in [32].

It is straightforward to implement UKF as real-time magnetometer calibration algorithm. First P, error covariance, is used to calculate set of sigma points,

$$\sigma_k \leftarrow \text{2n columns from} \pm \gamma\sqrt{P_k} \tag{3.30a}$$

$$\chi_k(0) = \hat{x}_k \tag{3.30b}$$

$$\chi_k(i) = \sigma_k(i) + \hat{x}_k \quad i = 1, 2, ..., 2n \tag{3.30c}$$

γ is given by $\gamma = \sqrt{n+\lambda}$, λ is the composite scaling factor in which $\lambda = \alpha^2(n+\kappa) - n$. The parameter α controls the spread of sigma points and is usually represented by small positive number, $(1 \times 10^{-4} \leq \alpha \leq 1)$ [32]. Moreover, κ is usually given by $\kappa = 3 - n$. Cholesky decomposition is used to compute the square root of a matrix [33]. We are using these parameters to define following weights,

$$W_0^{\text{mean}} = \frac{\lambda}{n+\lambda} \tag{3.31a}$$

$$W_0^{\text{cov}} = \frac{\lambda}{n+\lambda} + (1 - \alpha^2 + \beta) \tag{3.31b}$$

$$W_i^{\text{mean}} = W_i^{\text{cov}} = \frac{1}{2(n+\lambda)} \quad i = 1, 2, ..., 2n \tag{3.31c}$$

where β serves as the information for prior distribution.

Since we have the simplest system model, $\dot{\mathbf{X}} = 0$, propagation of state and covariances are rather straightforward and easy to calculate. In this case EKF and UKF formulation start to deviate from each other in the measurement update part especially in computation of innovation covariance. Here the first order expansion is used for EKF and nonlinear transformation is used for UKF.

TAM state estimation is calculated by,

$$\hat{x}_{k+1} = \hat{x}_k + K_k(z_{k+1} - \hat{z}_k) \tag{3.32}$$

mean observation $\hat{z}_k$ given by,

$$\hat{z}_k = \sum_{i=0}^{2n} W_i^{\text{mean}} h_{k+1}\left[\chi_k(i)\right] \tag{3.33}$$

where $h_{k+1}\left[\chi_k(i)\right]$ is the measurement model and defined in eq. 3.23. $h_{k+1}\left[\chi_k(i)\right]$ presents the evaluation at the $k+1$ time-step measurement using $\mathbf{B}_{k+1}$ and sigma point with $\chi_k(i)$. Corresponding Kalman gain is computed by,

$$K_k = P_k^{xz}\left[P_k^{xx} + \sigma_{k+1}^2(\hat{x}_k)\right]^{-1} \tag{3.34}$$

where P_k^{xz} is the cross-correlation matrix between $\hat{x}_k$ and $\hat{z}_k$ given by,

$$P_k^{xz} = \sum_{i=0}^{2n} W_i^{\text{cov}} \left[\chi_k(i) - \hat{x}_k\right] \left[h_{k+1}(\chi_k(i)) - \hat{z}_k\right]^T \tag{3.35}$$

and P_k^{zz} is the output covariance given by,

$$P_k^{zz} = \sum_{i=0}^{2n} W_i^{\text{cov}} \left[h_{k+1}(\chi_k(i)) - \hat{z}_k\right] \left[h_{k+1}(\chi_k(i)) - \hat{z}_k\right]^T \tag{3.36}$$

At the final step, estimated covariance can be found as,

$$P_{k+1} = P_k - K_k \left[P_k^{zz} + \sigma_{k+1}^2(\hat{x}_k)\right] K_k^T \tag{3.37}$$

Next iteration sigma points now can be calculated using the estimated covariance P_{k+1} for the recursive UKF.

CHAPTER 4

QUASI-MEASUREMENTS

This chapter, represents the main motivation of this thesis and proposes additional four quasi-measurements to be used for the magnetometer calibration on a spinning space vehicle. To derive these measurements we make use of the spinning spacecraft dynamics and specific behavior of magnetometer measurements for such spacecraft. We refer these measurements as quasi-measurements since they are not directly measured but rather derived from magnetometer measurements based under certain assumptions.

Derivation of quasi-measurements are conducted under three sections. In Section 4.1, two quasi measurements are derived using the spinning dynamic of the spacecraft. Third quasi measurement is obtained in Section 4.2 using the Geomagnetic Reference Field measurements based upon spacecraft orbit. Forth, the last, quasi-measurement derived in Section 4.3, uses the orthogonality property of magnetometer triad.

4.1 Angular Motion Originated Measurements

First we start with two of these quasi-measurements whose derivation is rather straightforward. Consider a spinning satellite rotating about the body Z axis with an angular rate ω as given in Fig. 4.1. The body Z-axis is referred as spin axis and the plane normal to this axis corresponds to spin plane. Working over (2.19) and expanding the relation where ($\bar{\mathbf{B}}_\mathbf{k} = A_k \mathbf{H}_\mathbf{k}$),

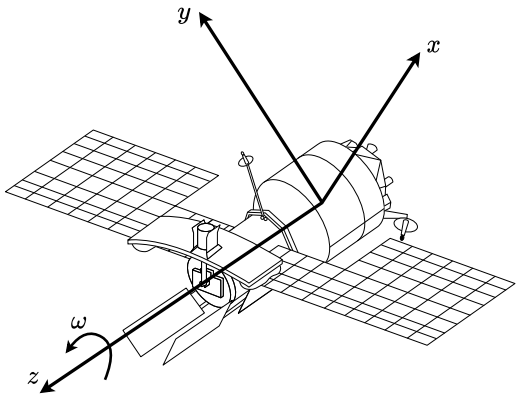

Figure 4.1: Spacecraft Motion Representation

$$\begin{bmatrix} 1+D_{11} & D_{12} & D_{13} \\ D_{21} & 1+D_{22} & D_{23} \\ D_{31} & D_{32} & 1+D_{33} \end{bmatrix} \begin{bmatrix} B_x \\ B_y \\ B_z \end{bmatrix} = \begin{bmatrix} \bar{B}_x \\ \bar{B}_y \\ \bar{B}_z \end{bmatrix} + \begin{bmatrix} b_x \\ b_y \\ b_z \end{bmatrix} + \begin{bmatrix} \epsilon_{\mathbf{x}} \\ \epsilon_{\mathbf{y}} \\ \epsilon_{\mathbf{z}} \end{bmatrix} \tag{4.1}$$

In the ideal case, when there is no sensor error, the measurements in the spin plane oscillate about zero-mean with 90° phase shift. Thus averaging the spin plane magnetometer measurements for a specified window length sweeps out the $[\bar{B}_x\ \bar{B}_y]^T$ terms and we are left with,

$$\begin{aligned} z_{2,k} &= \frac{1}{N}\sum B_x = \big(b_{x,k} - \frac{D_{12,k}}{N}\sum B_y - \frac{D_{13,k}}{N}\sum B_z\big)/\big(1+D_{11,k}\big) + \overline{\epsilon}_{\mathbf{x}} \\ z_{3,k} &= \frac{1}{N}\sum B_y = \big(b_{y,k} - \frac{D_{12,k}}{N}\sum B_x - \frac{D_{23},k}{N}\sum B_z\big)/\big(1+D_{22,k}\big) + \overline{\epsilon}_{\mathbf{y}} \end{aligned} \tag{4.2}$$

which are two of the new quasi-measurements that are used in the designed calibration algorithm. Here, $\overline{\epsilon}_x$ and $\overline{\epsilon}_y$ are Gaussian white noises as $\overline{\epsilon}_x, \overline{\epsilon}_y \sim N(0, \Sigma/N)$ and given with

$$\begin{aligned} \overline{\epsilon}_x &= \frac{1}{N}\sum \epsilon_x \\ \overline{\epsilon}_y &= \frac{1}{N}\sum \epsilon_y \end{aligned} \tag{4.3}$$

Further, applied filter is a moving average filter, in (4.2) and N is the window size.

Picking an appropriate window size is a critical decision. If the large window size is selected, the high frequency noise in the measurements can be reduced and estimation accuracy can be improved. However, using large windows is not practical for all applications since the algorithm becomes incapable of sensing variations in the estimated parameters. As will be discussed in the algorithm validation section, assigning a window size matching with the number of measurements within one spin period of the satellite is a reasonable choice. Nonetheless, this is not a strict requirement for the algorithm to work and can be relaxed depending on the sampling frequency of the magnetometers and the satellite's spin rate.

Thus far, we have formed two quasi measurements. For the Z-axis we cannot use same the intuition since there is no spin modulation for this axis. Instead we make use of fact that the spacecraft is purely spinning about the body Z axis and the spin-direction in the inertial frame is fixed (in the absence of any torque).

4.2 Constant Spin-axis Originated

In literature, the algorithms that are proposing attitude-independent magnetometer calibration using the gyro measurement (or relative angular position)[23, 24, 34] depends upon the approximation of $\dot{\mathbf{H}} \cong 0$, meaning that the change in reference inertial frame magnetic field vector is considerably small between two consecutive sampling steps. Assuming an error-free magnetometer the theory of using the angular velocity of the spacecraft for magnetometer calibration can be shown with the following steps. First let us show the measurements at two consecutive steps as (assuming $\mathbf{H_{k+1}} = \mathbf{H_k}$),

$$\mathbf{B_k} = A_k \mathbf{H_k} \tag{4.4}$$

$$\mathbf{B_{k+1}} = A_{k+1} \mathbf{H_k} \tag{4.5}$$

using $\mathbf{H_k} = A_k^T \mathbf{B_k}$ in equation (4.5) will give,

$$\mathbf{B_{k+1}} = A_{k+1} A_k^T \mathbf{B_k} \tag{4.6}$$

From the fundamental kinematic relations time derivative of the rotation matrix can be represented as,

$$\dot{A}_k = -\Omega(\omega) A_k \tag{4.7}$$

where $\Omega(\omega)$ is skew-symmetric matrix for ω,

$$\Omega(\omega) = \begin{bmatrix} 0 & -\omega_z & \omega_y \\ \omega_z & 0 & -\omega_x \\ -\omega_y & \omega_x & 0 \end{bmatrix}$$

Applying numeric time derivative for left side of (4.7),

$$\begin{aligned} \frac{A_{k+1} - A_k}{\Delta t} &= -\Omega(\omega) A_k \\ A_{k+1} &= [I_{3\times 3} - \Omega(\omega)\Delta t] A_k \\ A_{k+1} A_k^T &= [I_{3\times 3} - \Omega(\omega)\Delta t] \end{aligned} \tag{4.8}$$

Combining (4.6) and (4.8),

$$\mathbf{B_{k+1}} = [I_{3\times 3} - \Omega(\omega)\Delta t]\mathbf{B_k} \tag{4.9}$$

As a result we have

$$\frac{\mathbf{B_{k+1}} - \mathbf{B_k}}{\Delta t} = -\Omega(\omega)\mathbf{B_k} = \dot{\mathbf{B}}_\mathbf{k} \tag{4.10}$$

We derived the relations for perfect sensor measurement. It is straightforward to extend the derivation when there are sensor errors, however. Now recall the exploiting properties of skew-symmetric matrix, [e.g. $-\Omega(\omega)\mathbf{B_k} = \Omega(\mathbf{B_k})\omega$] and use (4.10) for satellite which has a pure spin about on body-Z axis.

$$\dot{\mathbf{B}}_\mathbf{k} = \Omega(\mathbf{B}_\mathbf{k}) \begin{bmatrix} 0 \\ 0 \\ \omega_{z,k} \end{bmatrix} = \begin{bmatrix} 0 & -B_{z,k} & B_{y,k} \\ B_{z,k} & 0 & -B_{x,k} \\ -B_{y,k} & B_{x,k} & 0 \end{bmatrix} \begin{bmatrix} 0 \\ 0 \\ \omega_{z,k} \end{bmatrix} \tag{4.11}$$

From (4.11) it is clear to see $\dot{B}_{z,k} = 0$. This is a fair assumption that can be used to derive a quasi-measurement for estimating the magnetometer biases, if no scaling and non-orthogonality is assumed. In contrast, in our experience, for a full calibration, it is not that useful and variation in the reference magnetic field vector distorts the estimation accuracy. For high sampling frequencies $\dot{\mathbf{H}}_\mathbf{k} = 0$ is still a valid assumption and a third quasi-measurement as $\dot{B}_{z,k} = 0$ can be used to aid the filter. Here we would like to derive a quasi-measurement which can be used even for low sampling frequencies (which is very likely for small satellites).

Now let us consider the case $\mathbf{H_{k+1}} \neq \mathbf{H_k}$ and add $\Delta\mathbf{H}$ over (4.5) where $\Delta\mathbf{H} = \mathbf{H_{k+1}} - \mathbf{H_k}$ which brings,

$$\mathbf{B_{k+1}} = A_{k+1}[\mathbf{H_k} + \Delta\mathbf{H}] \tag{4.12}$$

Rewriting (4.6) in the light of (4.12),

$$\mathbf{B_{k+1}} = A_{k+1}A_k^T\mathbf{B_k} + A_{k+1}\Delta\mathbf{H} \tag{4.13}$$

Now (4.10) becomes,

$$\frac{\mathbf{B_{k+1}} - \mathbf{B_k}}{\Delta t} = \dot{\mathbf{B}}_\mathbf{k} = -\Omega(\omega)\mathbf{B_k} + A_{k+1}\dot{\mathbf{H}}_\mathbf{k} \tag{4.14}$$

When we make $\dot{\mathbf{H}}_\mathbf{k} = 0$ assumption then we would have (4.10) indeed. Otherwise,

$$\dot{B}_{z,k} = 0 + A_{k+1}(3,1)\dot{H}_{x,k} + A_{k+1}(3,2)\dot{H}_{y,k} + A_{k+1}(3,3)\dot{H}_{z,k} \tag{4.15}$$

It is known that the last row of attitude matrix A_k gives inertial frame spin direction

as $\mathbf{X}_k = [x_s \ y_s \ z_s]$ which has constant terms if the satellite is performing pure spin motion without coning and/or nutation [35] .

$$A_k = \begin{bmatrix} . & . & . \\ . & . & . \\ x_s & y_s & z_s \end{bmatrix}$$

Thus,

$$\dot{B}_{z,k} = 0 + x_s\dot{H}_{x,k} + y_s\dot{H}_{y,k} + z_s\dot{H}_{z,k} \tag{4.16}$$

Now let use have the second derivative of $B_{z,k}$. Using the fact that spin-direction is constant it is clear that,

$$\ddot{B}_{z,k} = \underbrace{\dot{x}_s\dot{H}_{x,k}}_{=0} + x_s\ddot{H}_{x,k} + \underbrace{\dot{y}_s\dot{H}_{y,k}}_{=0} + y_s\ddot{H}_{y,k} + \underbrace{\dot{z}_s\dot{H}_{z,k}}_{=0} + z_s\ddot{H}_{z,k} \tag{4.17}$$

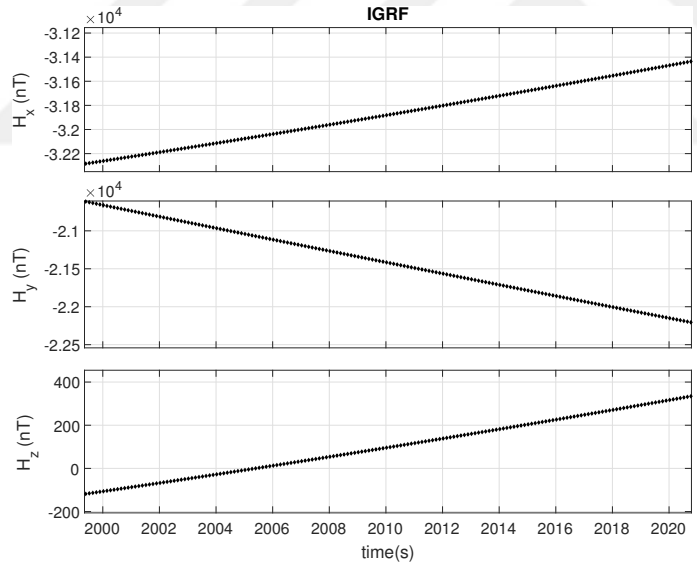

Figure 4.2: IGRF Data Portion

Thus we are left with the second derivatives of $\mathbf{H_k}$. Figure 4.2 shows the variation of reference magnetic field in inertial frame for Arase spacecraft about the perigee pass. Even for the long term variation for 20 seconds as given, it is clear that $\ddot{\mathbf{H}}_\mathbf{k} = 0$ is an assumption that holds true. So for a perfect magnetometer on a spinning spacecraft we shall have,

$$\ddot{B}_{z,k} = 0$$

Now departing from this fact, we can have the third quasi-measurement for a magnetometer that is corrupted with the bias, scaling and non-orthogonality.

$$z_{4,k} = \ddot{B}_{z,k} = \big(- D_{13,k}\ddot{B}_{x,k} - D_{23,k}\ddot{B}_{y,k}\big)/\big(1 + D_{33,k}\big) + \tilde{\epsilon}_z \tag{4.18}$$

In (4.10) $\tilde{\epsilon}_z$ presented as white noise.

4.3 Orthogonality Originated Measurement

Forth and the last quasi-measurement relies upon the time-shift in between the measurements of the spin plane magnetometers. Modern three-axis sensors are formed by stacking three single axis sensor in orthogonal fashion and aiming for best possible coverage in cartesian space. The assumption behind this measurement is rather straightforward: while the spacecraft is rotating about body z axis with an angular rate ω, in ideal (noise free) case magnetometer measurement in body x-axis should be equal to the quarter spin period previous measurement in y-axis, $\overline{B}_{x,k} \cong \overline{B}_{y,k-\frac{T}{4}} = \overline{B}_{y,k'}$ as seen in Figure 4.3. This intuition behind the forth quasi-measurement comes from the orthogonality of the sensing axes. It is assumed that the quarter spin period is short enough to disregard any variation in the magnetic field measurements due to the orbital position of the spacecraft. Starting from the expanded form of magnetometer measurement model and taking the first and second to work over relation (eq. 4.1),

$$\begin{aligned}
\overline{B}_{x,k} &= \overline{B}_{y,k'} \\
\overline{B}_{x,k} &= (1 + D_{11,k})B_{x,k} + D_{12,k}B_{y,k} + D_{13,k}B_{z,k} - b_{x,k} \\
\overline{B}_{y,k'} &= D_{21,k'}B_{x,k'} + (1 + D_{22,k'})B_{y,k'} + D_{23,k'}B_{z,k'} - b_{y,k'}
\end{aligned} \tag{4.19}$$

Rearranging (4.19) and considering $(k' = k - \frac{T}{4})$,

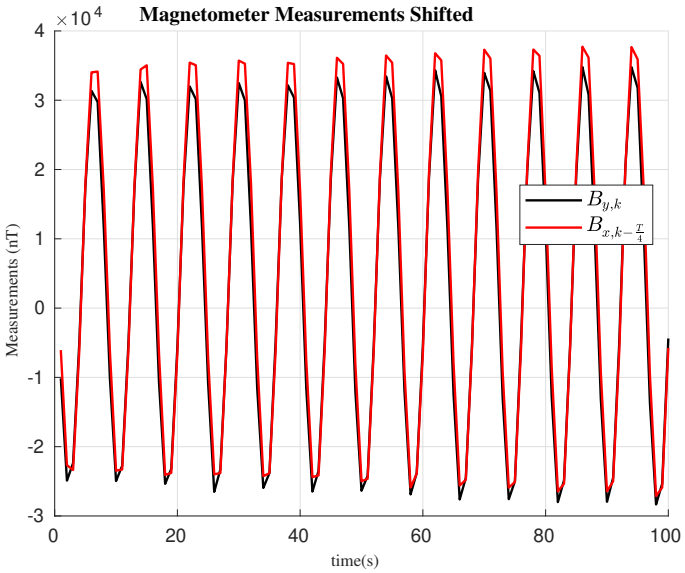

Figure 4.3: Spin Planar Measurements for an Error Free Magnetometer when Body X Axis Measurements are quarter spin period shifted

$$z_{5,k} = B_{x,k} = \big(D_{21,k'}B_{x,k'} + (1 + D_{22,k'})B_{y,k'} + D_{23,k'}B_{z,k'} - b_{y,k'} - D_{12,k}B_{y,k} - D_{13,k}B_{z,k} + b_{x,k}\big)/(1 + D_{11,k}) + \tilde{\epsilon}_x \tag{4.20}$$

Finally, assuming that the error terms are not changing within $(\frac{T}{4})$ time interval,

$$z_{5,k} = B_{x,k} = \big(D_{21,k}B_{x,k'} + (1 + D_{22,k})B_{y,k'} + D_{23,k}B_{z,k'} - b_{y,k} - D_{12,k}B_{y,k} - D_{13,k}B_{z,k} + b_{x,k}\big)/(1 + D_{11,k}) + \tilde{\epsilon}_x \tag{4.21}$$

In eq. 4.20 and 4.21, $\tilde{\epsilon}_x$ presented as white noise.

This concludes the derivation of four quasi-measurements. Combining with the attitude independent observation we have five measurements to be used in the proposed estimation algorithm.

CHAPTER 5

SIMULATION AND RESULTS

In this chapter, proposed magnetometer calibration algorithm with quasi-measurements is evaluated with both simulated data for hypothetical spacecraft and real magnetometer data from ERG spacecraft of JAXA. To compare the accuracy, same tests are repeated with the TWO-STEP algorithm [21] and the UKF with a single measurement given in [18].

Although, Crassidis stated that EKF algorithm diverges. To show improvements of quasi-measurements. Results for EKF with 5 measuruments are also presented.

The proposed EKF and UKF with 5 measurements has the state vector of,

$$\mathbf{X} = [b_x \; b_y \; b_z \; D_{11} \; D_{22} \; D_{33} \; D_{12} \; D_{13} \; D_{23}]^T \tag{5.1}$$

and the measurements of $\mathbf{Z}_{1-5}$ from equations (3.23, 4.2, 4.18, 4.21). The system model in the filter assumes all the estimated states are constant as $(\dot{\mathbf{X}} = 0)$.

Both EKF and UKF algorithms are executed with same initialization set of process noise covariance, Q, measurement noise covariance, R, and initial error covariance, P_0. Process noise covariance, Q, for the filter is given as,

$$Q = \text{diag}\left(10^{-8} \times \text{ones(1,3)}, \quad 10^{-12} \times \text{ones(1,6)}\right) \tag{5.2}$$

Measurement noise covariance, R, for the filter is given as,

$$R = \text{diag}\left(8 \times 10^{15},\ \ 5 \times 10^{5},\ \ 5 \times 10^{5},\ \ 1 \times 10^{11},\ \ 1 \times 10^{9}\right) \tag{5.3}$$

Initial error covariance, P_0 is taken as,

$$P_0 = \text{diag}\left((3 \times 10^{6}) \times \text{ones(1,3)},\ \ (1 \times 10^{-1}) \times \text{ones(1,6)}\right) \tag{5.4}$$

5.1 Results for Simulated Dataset

5.1.1 Simulation Environment

For simulation phase, the algorithm is tested for a hypothetical spinning nano-satellite whose orbit is assumed to be LEO with a small eccentricity of $e = 6.4 \times 10^{-5}$, inclination of $i = 74$ deg and an approximate altitude of 612 km, Celestial orbital elements are illustrated in Fig 5.1. The orbital plane denoted with yellow, intersects with gray colored reference plane. Earth's equatorial plane serves as reference plane for Earth orbiting satellites. The satellite spins about its body Z-axis with a spin rate of 7.5 rpm. Orbit of the satellite propagated using Newton's equation 5.5,

$$\ddot{\mathbf{r}} = -GM\frac{\mathbf{r}}{r^3} + f_p(t, r, \dot{r}, ...) \tag{5.5}$$

Here G is the gravitational constant, M is Earth's mass, **r** is the position vector in ECI, r is the distance to the Earth's center and finally $f_p(t, r, \dot{r}, ...)$ is the all perturbing forces that depend on time, position, velocity and satellite's shape. However, for the sake of simplicity perturbation effects are neglected at this point of the study.

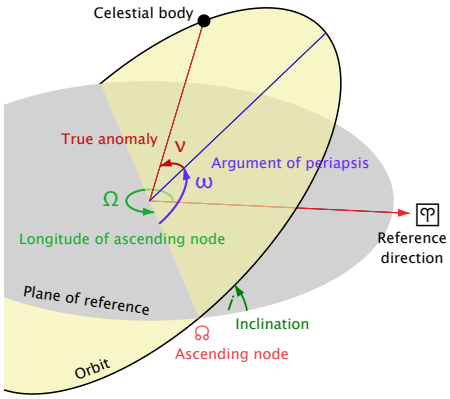

Figure 5.1: Keplerian Orbital Elements [7]

For the magnetometer measurements, the sensor noise is characterized by zero mean Gaussian white noise with standard deviation of $\sqrt{\Sigma} = 300\,nT$. Magnetometer errors are assumed to be constant and actual values are given in Table 5.1. Initial portion of simulated measurements are given in Fig. 5.2. Simulations run for 36000 s, which corresponds to approximately six orbital revolution of satellite, and the sampling time (both for the filter propagation and measurements) is $\Delta t = 1\,s$. Window size (N) is selected as eight samples, which is exactly one spin period. This is an ideal value because it matches with the spin period and is small enough to sense variations.

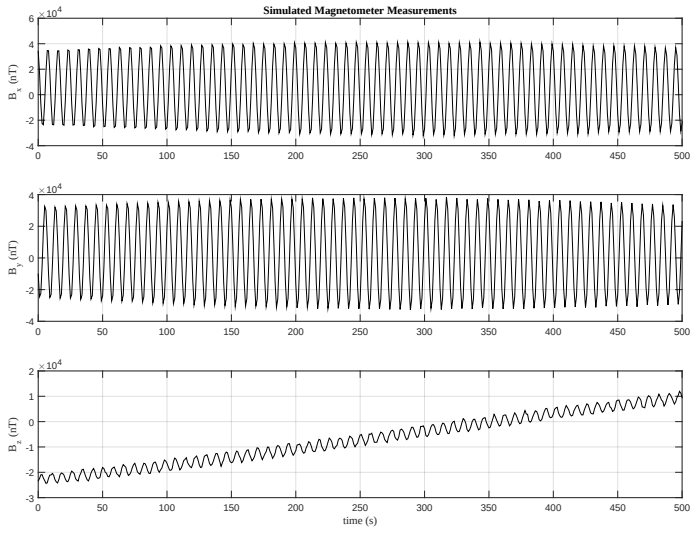

Figure 5.2: Simulated Measurements for Hypothetical Nano-Satellite

5.1.2 Reference Algorithms Result

To serve benchmark for the upcoming quasi-measurement, simulated data is first evaluated with the UKF with 1 measurements, attitude independent measurement only eq. 3.23. Although, Crassidis [18] stated divergence problems, simulated data also evaluated with EKF with 1 measurement and finally with batch TWO-STEP algorithm. Results are given in Figures 5.3-5.5. Figures include only the recursive algorithm results. Since TWO-STEP is a batch algorithm, discussed in Table 5.1.

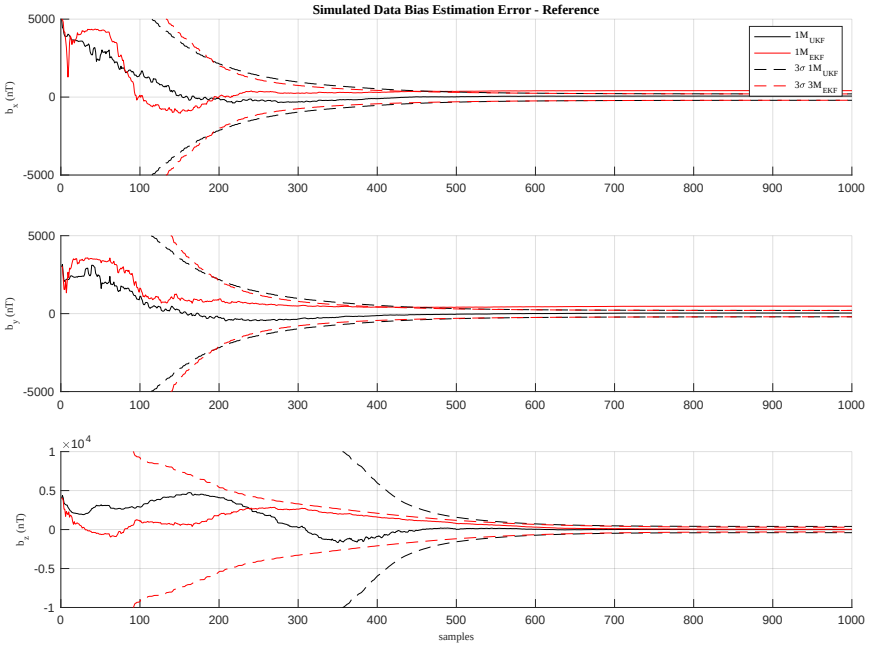

Figure 5.3: Reference Bias Estimation Errors for Simulated Data and 3σ Bounds

Although, Crassidis stated divergence problems, EKF algorithm could converge with the simulated data.

Bias states, b_x and b_y converge with similar rate in both algorithms with close 3σ bounds but EKF shows more oscillatory convergence compared to UKF. On Z axis bias, b_z, convergence of 3σ bound is considerably fast with EKF algorithm. On each bias states EKF and UKF algorithm show similar transient behaviors, and deviate with steady state accuracy. EKF could not show superior performcance like UKF

algorithm.

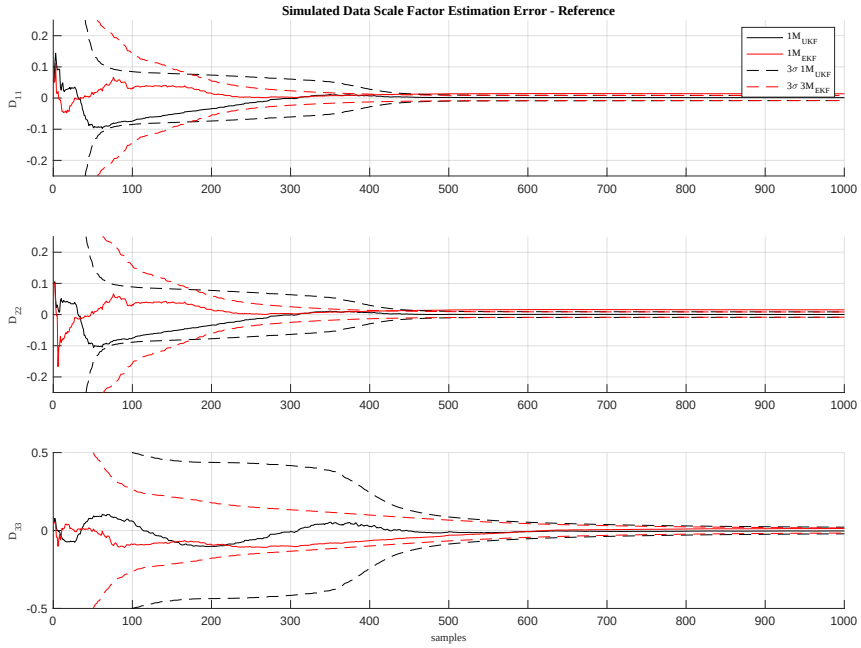

Figure 5.4: Reference Scale-Factor Errors for Simulated Data and 3σ Bounds

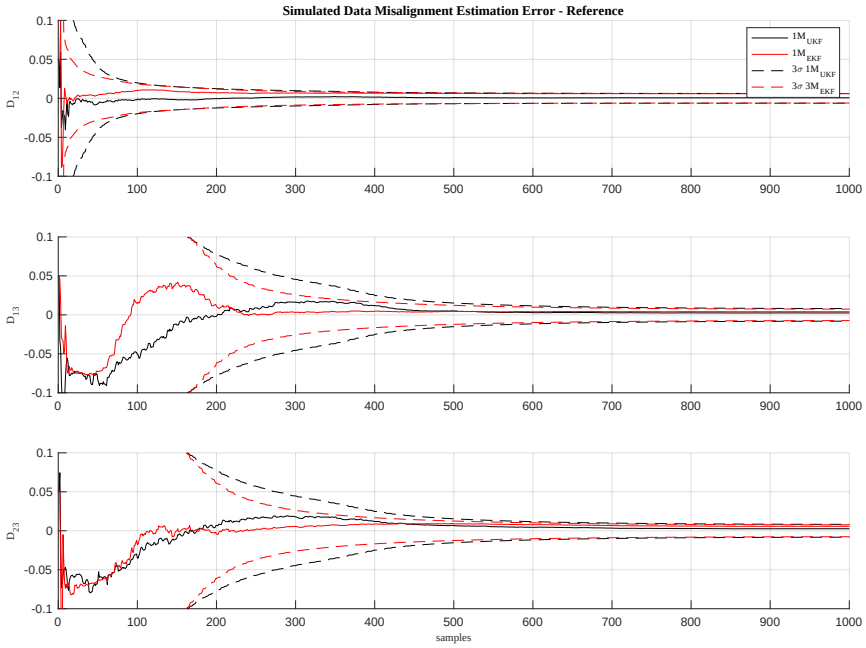

Figure 5.5: Reference Misalignment Errors for Simulated Data and 3σ Bounds

Similar performance also valid in scale-factor and misalignment states. EKF algorithm shows faster decreasing 3σ bounds in Z axis states. To compare steady state accuracy of the reference algorithms, 1000 run Monte-Carlo simulation is conducted and results are given in Table 5.1.

Table 5.1: Reference Algorithms Monte-Carlo Result for Simulated Data

Parameter	Actual Value	TWO-STEP	EKF 1-Measurement	UKF 1-Measurement
$\mathbf{b_x}$	5000 nT	$4998.6599 \pm 11.1853\,nT$	$4565.2233 \pm 11.3755\,nT$	$4997.3553 \pm 11.2589\,nT$
$\mathbf{b_y}$	3000 nT	$2999.0310 \pm 10.7930\,nT$	$2481.7172 \pm 10.7509\,nT$	$2998.0893 \pm 10.8885\,nT$
$\mathbf{b_z}$	4000 nT	$4007.9321 \pm 8.5014\,nT$	$3880.6026 \pm 9.1391\,nT$	$4007.8159 \pm 8.5488\,nT$
$\mathbf{D_{11}}$	0.05	0.0497 ± 0.0005	0.0314 ± 0.0005	0.0497 ± 0.0005
$\mathbf{D_{22}}$	0.1	0.0996 ± 0.0005	0.0793 ± 0.0005	0.0996 ± 0.0005
$\mathbf{D_{33}}$	0.05	0.0496 ± 0.0003	0.0305 ± 0.0003	0.0496 ± 0.0003
$\mathbf{D_{12}}$	0.05	0.0499 ± 0.0004	0.0460 ± 0.0004	0.0500 ± 0.0004
$\mathbf{D_{13}}$	0.05	0.0499 ± 0.0003	0.0469 ± 0.0003	0.0499 ± 0.0003
$\mathbf{D_{23}}$	0.05	0.0499 ± 0.0003	0.0460 ± 0.0003	0.0499 ± 0.0003

Results show that, UKF algorithm with 1 measurement reaches superior performance with TWO-STEP algorithm. On the other hand, EKF could reach similar 3σ bounds but there are significant steady state accuracy problems are happened which means, first order approximation of the measurement model could not keep up with the highly nonlinear dynamics. Performance of the EKF algorithm will also evaluated with additional quasi-measurements in subsection 5.1.3 to check for any improvements. Since EKF requires less system resources compared to UKF algorithm [31] and this property make it more suitable for on-board applications.

5.1.3 Quasi-Measurements Result

Simulated data is evaluated with the proposed UKF with 5 measurements, UKF with 3 measurements (Z_{1-2} only) and the reference methods of the UKF with 1 measurement (attitude independent) and batch TWO-STEP algorithm. In order to check for any improvement, enhanced EKF algorithm with 5 measurements is also evaluated.

In Figure 5.6-5.8 magnetometer estimation errors are plotted with their $\pm 3\sigma$ bounds.

In figures the proposed algorithm is labelled as ($5M_{UKF}$) whereas the intermediate UKF algorithm with ($3M_{UKF}$) and reference UKF algorithm with only attitude-independent measurements is labelled with ($1M_{UKF}$). Finally, enhanced 5 measurement EKF is given with ($5M_{EKF}$). As seen in figures, with new quasi-measurements convergence rate and accuracy have increased in all states. Especially for x and y channel bias states; b_x, b_y very quick convergence occurred which is expected since first two quasi-measurements (eq. 4.2) considerably improves the observability of these states.

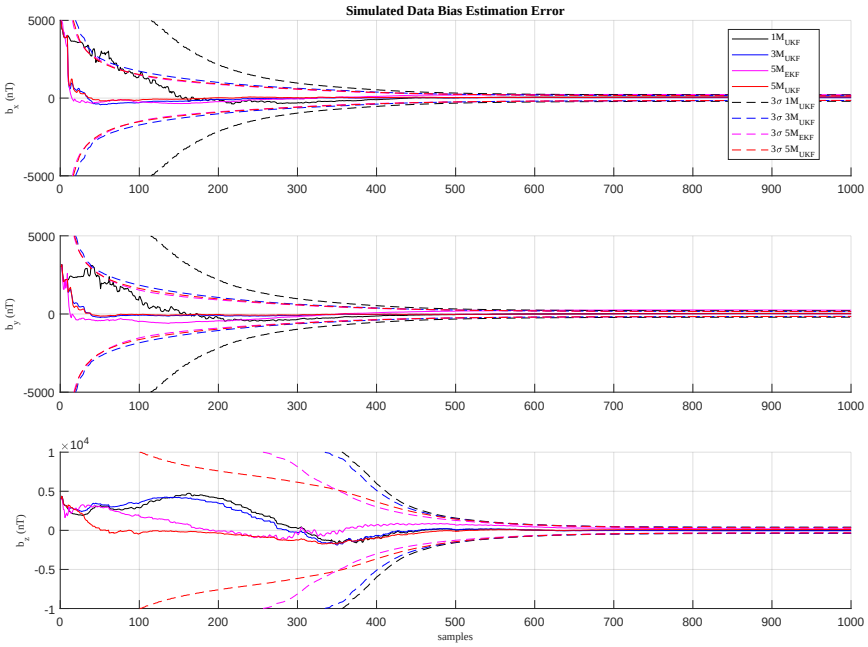

Figure 5.6: Bias Estimation Errors for Simulated Data and 3σ Bounds

Another considerable change is observed in XZ and YZ channel miaslignment states; D_{13}, D_{23}. D_{12} had already a better observability compared to D_{13} and D_{23}. Moreover in all states, convergence rate improvement can be seen as faster with faster decreasing covariance bounds. Lower covariance bounds for UKF with (5M) is visible once the filters converge to the steady state. Additional quasi measurement helped to eliminate overshoots in b_z, D_{11}, D_{12}, D_{22}, D_{13} and D_{23} states.

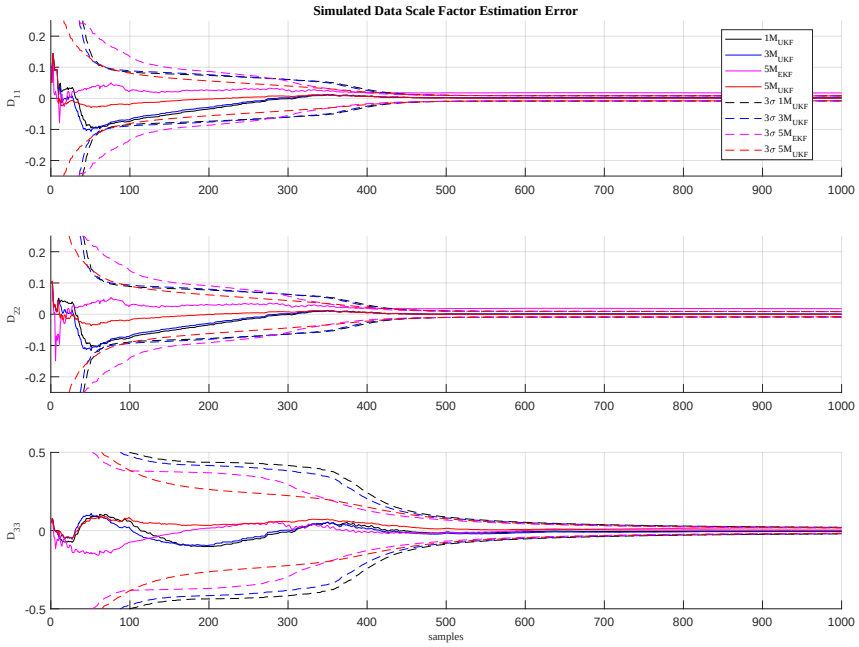

Figure 5.7: Scale-Factor Estimation Errors for Simulated Data and 3σ Bounds

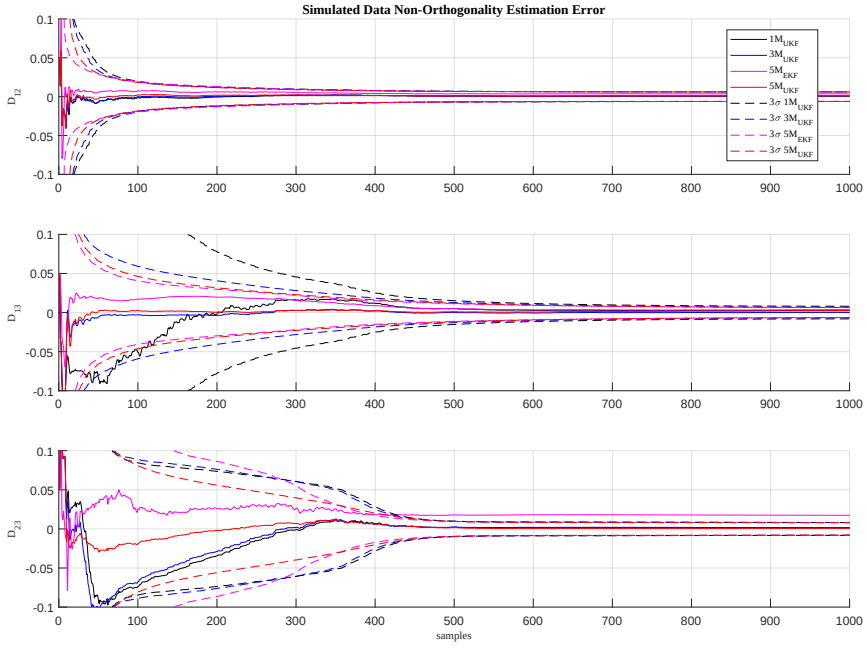

Figure 5.8: Non-orthogonality Estimation Errors for Simulated Data and 3σ Bounds

Estimation convergence accuracy can also be illustrated with Figure 5.9 and 5.10.

where Figure 5.9 gives the residuals for real-time estimates and Figure 5.10 is given with the final converged state to compare algorithm performance for steady state and compare against TWO-STEP algorithm. As seen on both figures, since error terms assumed to be constant residual values converge to sensor noise figure. Measurement model for the EKF algorithm could not show superior performance even with additional quasi measurements. Residuals were left in the measurement innovations. In order to give clear figures, both figures are filtered with 100 bank moving average filter.

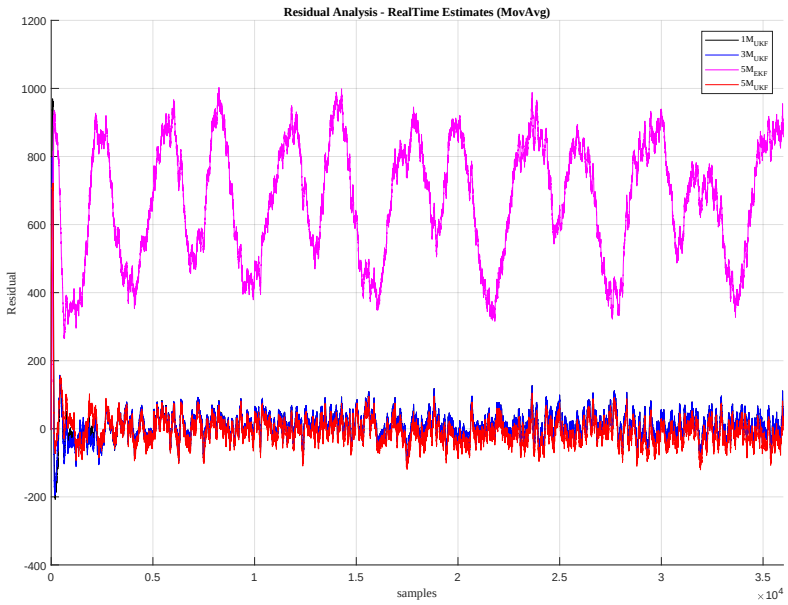

Figure 5.9: Simulated Data Residuals for Real-Time Estimates (Filtered)

To compare proposed algorithm performance in more analytical manner, 1000 run Monte-Carlo analysis was conducted. Their last converged estimation values and the calculated $\pm 3\sigma$ values are given in Table 5.1. This study aims steady state performance for proposed calibration algorithm. As seen in the table, major improvement due to quasi-measurements are in the b_x and b_y bias states. Overall state accuracy both in terms of the mean values and the convergence rate of $\pm 3\sigma$ bounds are considerably increased, specifically compared to the UKF with 1 measurement. Even though for

two of the states (D_{33} and D_{12}) the mean values are slightly worse compared to the UKF with 1M, the $\pm 3\sigma$ values are more important since they represent the variability of the Monte-Carlo simulations.

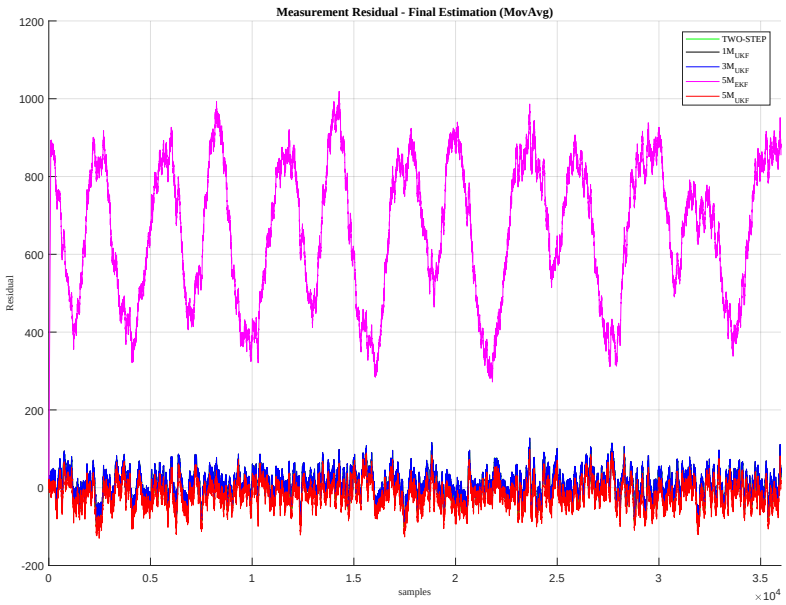

Figure 5.10: Simulated Data Residuals for Final Estimates (Filtered)

Table 5.2: Quasi-Measurements Monte-Carlo Result for Simulated Data

Parameter	**Actual Value**	**UKF 3-Measurement**	**EKF 3-Measurement**	**UKF 5-Measurement**
$\mathbf{b_x}$	5000 nT	$4998.4317 \pm 7.1401\, nT$	$4836.9144 \pm 7.0572\, nT$	$4997.6294 \pm 7.1448\, nT$
$\mathbf{b_y}$	3000 nT	$2998.7552 \pm 7.0821\, nT$	$2833.7308 \pm 7.1233\, nT$	$2998.3842 \pm 7.0840\, nT$
$\mathbf{b_z}$	4000 nT	$4008.3975 \pm 8.5471\, nT$	$3879.1623 \pm 8.7993\, nT$	$4008.2667 \pm 8.5574\, nT$
$\mathbf{D_{11}}$	0.05	0.0497 ± 0.0005	0.0281 ± 0.0005	0.0497 ± 0.0005
$\mathbf{D_{22}}$	0.1	0.0996 ± 0.0006	0.0775 ± 0.0005	0.0996 ± 0.0006
$\mathbf{D_{33}}$	0.05	0.0496 ± 0.0003	0.0293 ± 0.0003	0.0496 ± 0.0003
$\mathbf{D_{12}}$	0.05	0.0499 ± 0.0004	0.0458 ± 0.0004	0.0499 ± 0.0004
$\mathbf{D_{13}}$	0.05	0.0500 ± 0.0003	0.0460 ± 0.0002	0.0499 ± 0.0003
$\mathbf{D_{23}}$	0.05	0.0499 ± 0.0003	0.0457 ± 0.0003	0.0499 ± 0.0003

Clearly including the quasi-measurements decreases the bounds for all the states. The UKF with 5M provides competitive results with the batch TWO-STEP algorithm. As

a result of quasi-measurement of (eq. 4.2) the b_x and b_y states are more accurately estimated even compared to the TWO-STEP. EKF with 5 measurement has better transient performance compared to reference algorithm but steady state accuracy is not good enough for operational use.

5.2 Results for Real Dataset

In this section, proposed algorithm is evaluated for the magnetometer data collected by ERG (Exploration of energization and Radiation in Geospace) spacecraft of JAXA. For comparison estimation results by well-known batch TWO-STEP algorithm, enhanced EKF with 5 measurement, the UKF with 1 measurement and UKF with 3 measurement are presented.

5.2.1 Satellite & Orbital Properties

ERG is Sun-oriented and spin-stabilized about the major-axis with 7.5rpm spin rate (spin period of 8s). Rendered illustration presented in Fig. 5.11. The spin-axis, which is defined as the body Z axis, is required to be $5 - 10^{\circ}$ off of the Sun direction. The spacecraft weighs about 350kg. Since launch it has been performing its mission at highly elliptical orbit which has a perigee about 440 km and apogee about 32,000 km. One orbital period lasts about 9.5h. The orbit inclination is 32° [36].

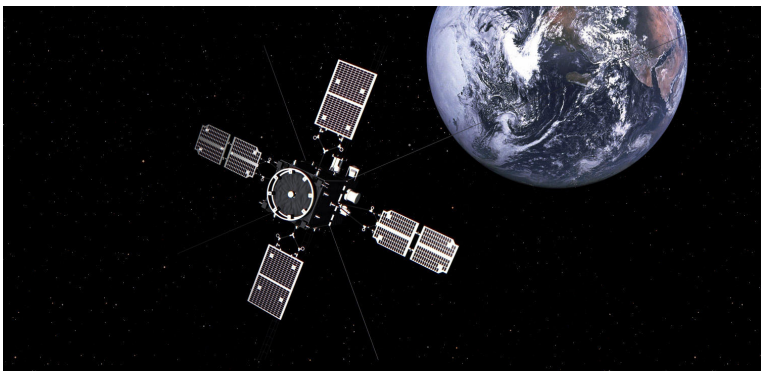

Figure 5.11: Exploration of energization and Radiation in Geospace "ARASE" (ERG) Satellite

Here the proposed algorithm is tested for the magnetic field measurements collected by a three-axis Geomagnetic Aspect Sensor (GAS) located on-board the spacecraft. The GAS measurements are used for coarse attitude estimation and the TWO-STEP estimates have been used actively for calibrating the sensor data since the launch [37]. The measurement data seen in Fig. 5.12 is for the early stages of the operation and presents approximately 3h portion of one orbital revolution.

Testing the proposed algorithm with real data collected by the ERG gives us also the chance to evaluate its performance in a more generic case. Due to the flexible appendages, the ERG spacecraft's major principal axis is not matching with the body Z axis, which is also the intended spin axis. Moreover, due to the attitude control maneuvers about the perigee passes to align the spacecraft's spin-axis with the Sun direction, nutations are observed [37]. Thus, the assumptions for a magnetometer triad perfectly aligned with the spin direction and the spin plane is no more valid in practice.

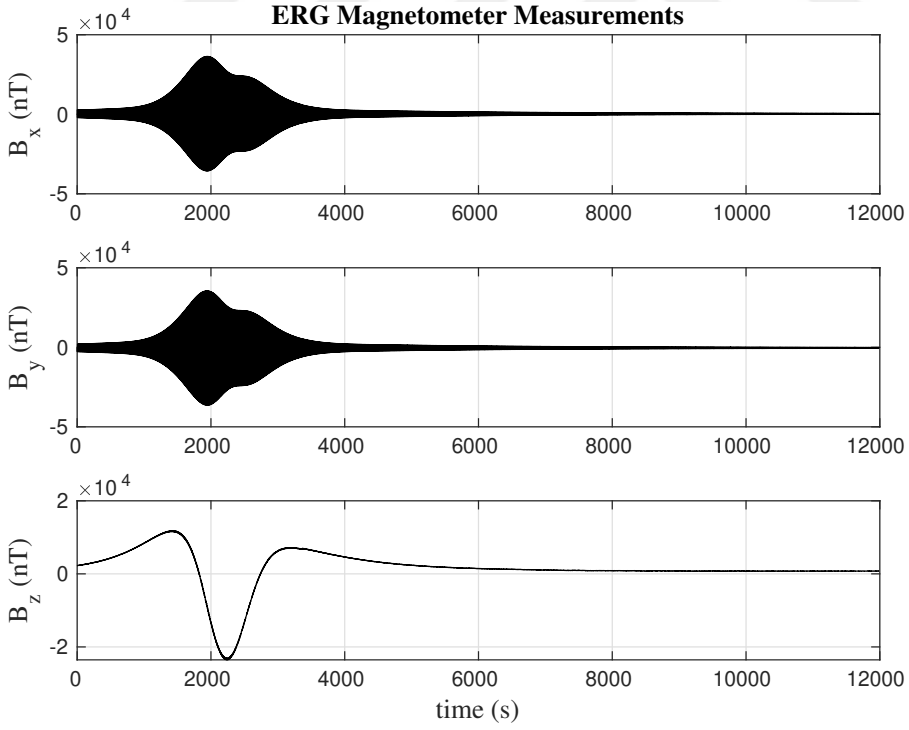

Figure 5.12: ERG Magnetometer Measurements

5.2.2 Reference Algorithms Result

As seen in Figure 5.12, magnitude of the measured magnetic field reaches to maximum at about 2000 s which corresponds to the perigee pass of the satellite. This information is critical since this is also where we have highest residuals and the filter is very sensitive against the variations. Results of all tested algorithms are summarized in Table 5.4. Being not capable of sensing the real-time variations and low observability conditions during approach to the apogee have detrimental effects on the TWO-STEP results and when the entire dataset is used it cannot converge. Thus, perigee pass portion is cropped out and used to achieve successful convergence with TWO-STEP algorithm.

Reference EKF algorithm also could not keep up with the increased residuals during perigee pass and having struggle with divergence. Addition of new quasi measurements increases EKF algorithm robustness, by that way algorithm could survive and satisfy convergence.

Table 5.3: Reference Algorithms Result with Real Data

Parameter	**TWO-STEP**	**UKF 1-Measurement**
$\mathbf{b_x}$	$299.5010\,nT$	$-473.1841\,nT$
$\mathbf{b_y}$	$-377.9110\,nT$	$-239.9346\,nT$
$\mathbf{b_z}$	$762.3921\,nT$	$-96.8622\,nT$
$\mathbf{D_{11}}$	0.0023	-1.9429
$\mathbf{D_{22}}$	0.0041	-0.0542
$\mathbf{D_{33}}$	0.0043	0.0265
$\mathbf{D_{12}}$	0.0021	0.3892
$\mathbf{D_{13}}$	0.0028	0.0047
$\mathbf{D_{23}}$	0.0004	-0.00005

Real-time performance of the UKF with 1 measurement also presented between Figures 5.13 and 5.15.

5.2.3 Quasi-Measurements Result

As to the UKF with 5 measurements, it also converges to almost same values with those of TWO-STEP except the D_{33}. D_{13} and D_{23} states. However, new 5-measurement UKF algorithm seems more robust against increased residual conditions and resists against divergence unlike UKF with 1-measurement. Also estimation accuracy is greater compared to UKF with 3-measurements. Similar to what we have seen in simulation results, quasi-measurements, considerably increase the convergence rate for X and Y channel bias states; b_x, b_y (Fig. 5.13.). We can also observe minor changes for XZ non-orthogonality state, D_{13} (Fig. 5.14.).

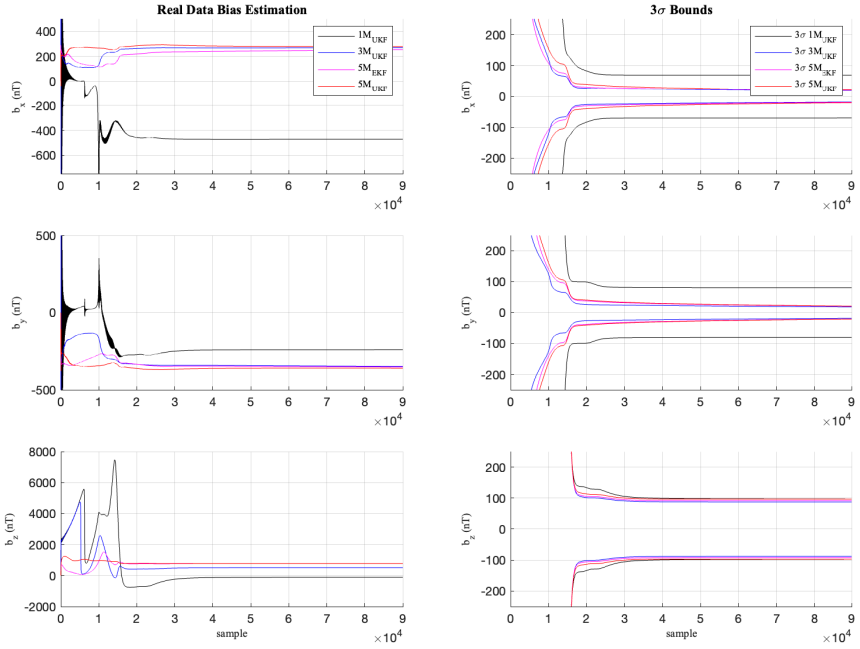

Figure 5.13: Real Data Bias Estimation and 3σ Bounds

When we consider the results for simulated and real data together, incorporating the quasi-measurements improve the robustness of the UKF for real-time magnetometer calibration on a spinning spacecraft. The proposed algorithm consistently provides better estimates compared to the TWO-STEP and the UKF with ($1M_{UKF}$). Unlike the TWO-STEP algorithm, it is real-time applicable and capable of sensing any possible variations in the estimated error terms.

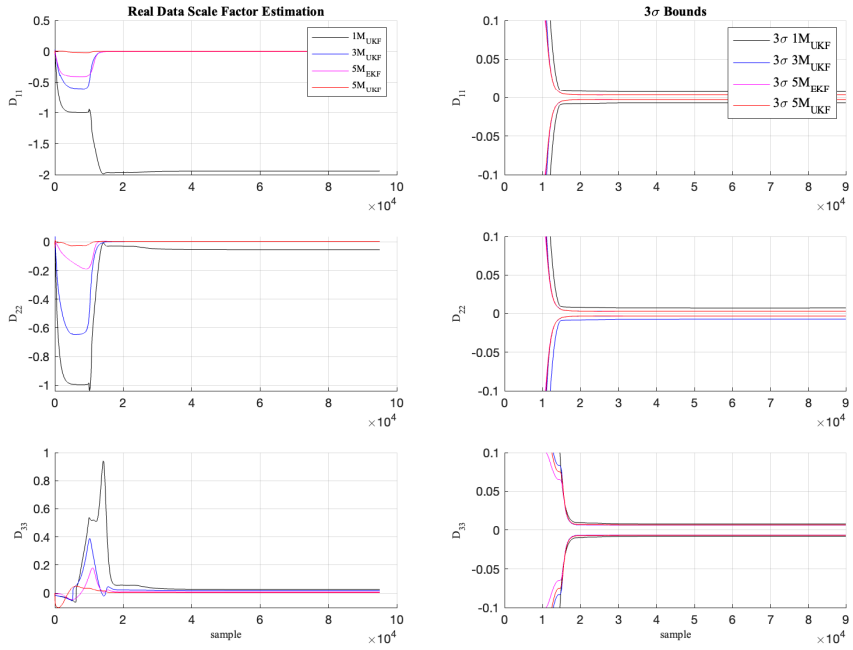

Figure 5.14: Real Data Scale-Factor Estimation and 3σ Bounds

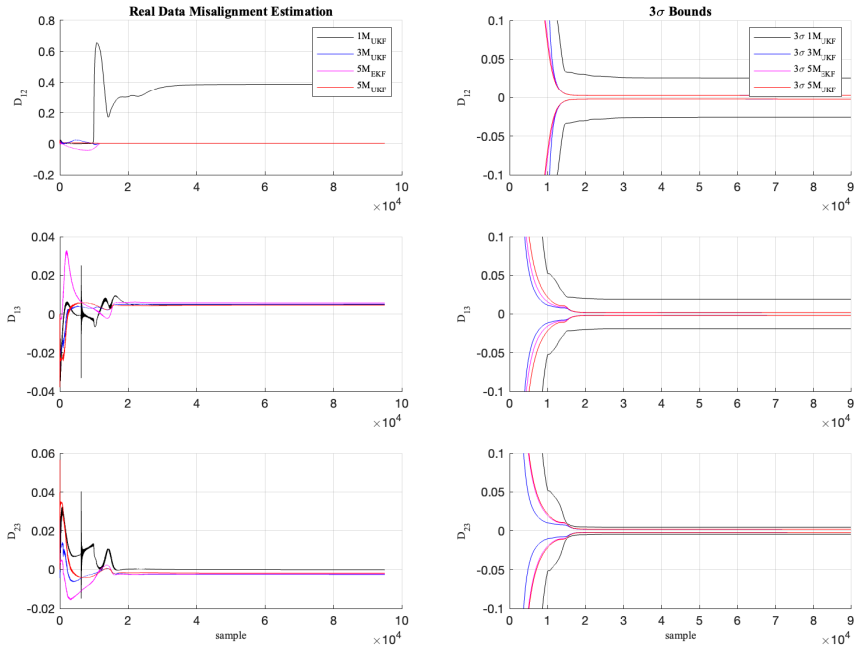

Figure 5.15: Real Data Misalignment Estimation and 3σ Bounds

Table 5.4: Quasi-Measurements Result with Real Data

Parameter	UKF 3-Measurement	EKF 5-Measurement	UKF 5-Measurement
$\mathbf{b_x}$	$271.5324\,nT$	$254.7285\,nT$	$278.4135\,nT$
$\mathbf{b_y}$	$-348.5022\,nT$	$-352.4138\,nT$	$-358.1898\,nT$
$\mathbf{b_z}$	$506.2751\,nT$	$773.7024\,nT$	$704.6716\,nT$
$\mathbf{D_{11}}$	0.0018	-0.0034	0.0021
$\mathbf{D_{22}}$	0.0036	0.0040	0.0040
$\mathbf{D_{33}}$	0.0186	0.0083	0.0076
$\mathbf{D_{12}}$	0.0021	0.0022	0.0021
$\mathbf{D_{13}}$	0.0050	0.0057	0.0047
$\mathbf{D_{23}}$	-0.0025	-0.0022	-0.0019

To better evaluate the algorithms with the real data we analyzed the residuals (measurement innovations) that the estimated magnetometer errors produce. It is simply the difference of the norm of the calibrated measurements and the magnetic field reference vector. Figure 5.16 and 5.17 gives the residuals corresponding to the real-time and final estimates respectively, errors in Figures 5.13-5.15 for UKF algorithms. Residual plots are filtered with 100 bank moving average filter for clear discussion. TWO-STEP results excluded since it could only offer post processed estimates. Therefore its performance is given in Figure 5.17. We see that the residual for the UKF with ($5M_{UKF}$) is lesser compared to the UKF with ($1M_{UKF}$) and UKF with ($3M_{UKF}$). The UKF with (1M) algorithm diverges during the perigee pass and due to steeply increasing residuals, individual errors cannot be differentiated. After the perigee passage, the UKF (1M) filter has already been converged to certain values and the small covariance values make it unable to correct false convergence, unless the filter is excited by artificially increasing the state estimation covariances. UKF with ($3M_{UKF}$) algorithm gave much promising results but not good as proposed algorithm with ($5M_{UKF}$). As a result the algorithm converges to different values compared to the TWO-STEP. Proposed algorithm shows nearly same performance for steady state accuracy compared to TWO-STEP results, given in Figure 5.17.

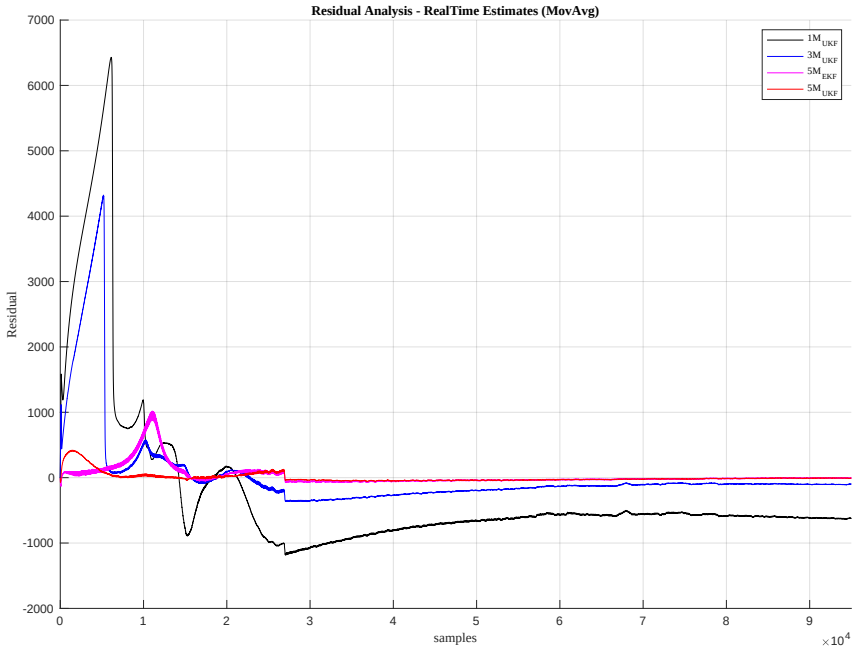

Figure 5.16: Real Data Residuals for Real-Time Estimates (Filtered)

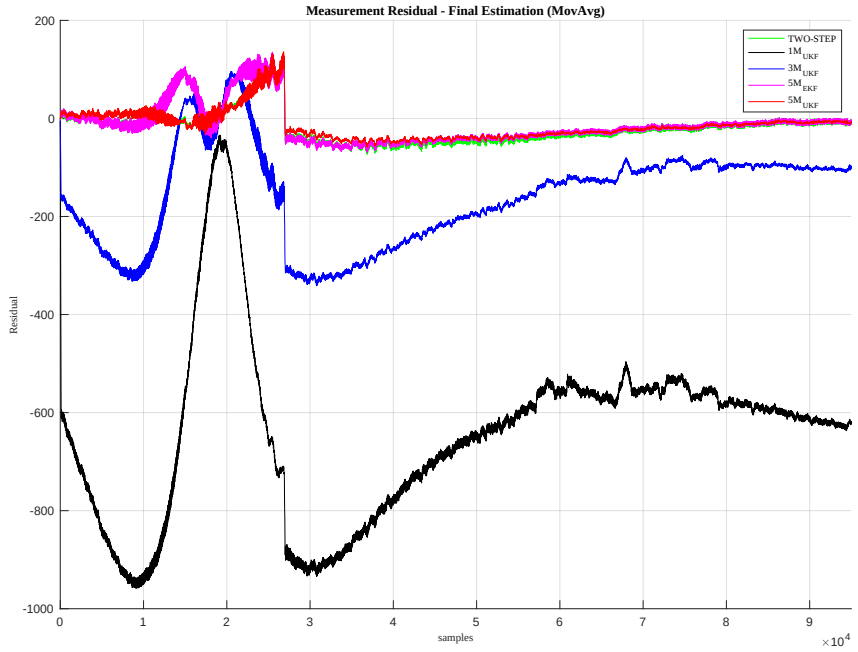

Figure 5.17: Real Data Residuals for Final Estimates (Filtered)

Additional quasi-measurements increased the robustness of the EKF with 5 measurements ($5M_{EKF}$). Under that condition, EKF could show similar transient behavior with $5M_{UKF}$. However, due to lack of modelling nonlinear dynamics, EKF algorithm could not show superior performance compared to UKF algorithm. To see clearly we can check Figures 5.16 and 5.17, EKF has greater norm for the residuals during perigee pass and even for steady state conditions.

CHAPTER 6

CONCLUSION AND FUTURE WORK

6.1 Conclusion

In this thesis, a real-time attitude independent magnetometer calibration algorithm is proposed for spinning spacecraft. The recursive estimator is formulated as an Unscented Kalman Filter (UKF) and Extended Kalman Filter (EKF). Four new quasi-measurements, which are derived using dynamic characteristics of the spacecraft, are introduced and used in the filtering algorithm in addition to the attitude-independent scalar measurement of TWO-STEP algorithm. The proposed algorithm is evaluated with both simulated and real spacecraft data. Results are compared with those of three benchmark algorithms, including the UKF and EKF that uses only the scalar measurement.

Results show that new quasi-measurements considerably improve the observability and heals convergence characteristics of the filter as well as the estimation accuracy for UKF and EKF algorithms. However, due to high nonlinear dynamics, EKF algorithm is having struggle to satisfy steady state accuracy performance. Therefore, beside processing load using UKF with proposed quasi-measurements for real-time magnetometer calibration is recommended.

6.2 Future Work

As future work, following tasks were planned.

- Proposed algorithm will be evaluated with time-varying errors. Hypothetical

spacecraft measurements were generated assuming that magnetometer errors were constant. So far we've shown mostly the steady state performance of the filter. This study will serve the performance for tracking capabilities.

- In moving average quasi-measurement eq. 4.2, fixed window length was used since spacecraft angular rate is almost constant for hypothetical and real spacecraft data. However, this wouldn't be the case for real-world applications. Adaptive window length can also be implemented by using well known Kalman Frequency tracker algorithm [38].

REFERENCES

[1] P. Alken, E. Thébault, C. D. Beggan, H. Amit, J. Aubert, J. Baerenzung, T. Bondar, W. Brown, S. Califf, A. Chambodut, *et al.*, "International geomagnetic reference field: the thirteenth generation," *Earth, Planets and Space*, vol. 73, no. 1, pp. 1–25, 2021.

[2] Wikipedia, "Earth-centered inertial — Wikipedia, the free encyclopedia." http://en.wikipedia.org/w/index.php?title=Earth-centered%20inertial&oldid=1054096556, 2021. [Online; accessed 20-September-2021].

[3] Wikipedia, "Local tangent plane coordinates — Wikipedia, the free encyclopedia." http://en.wikipedia.org/w/index.php?title=Local%20tangent%20plane%20coordinates&oldid=1063628292, 2021. [Online; accessed 30-August-2021].

[4] C. H. Acton Jr, "Ancillary data services of nasa's navigation and ancillary information facility," *Planetary and Space Science*, vol. 44, no. 1, pp. 65–70, 1996.

[5] A. Noureldin, T. B. Karamat, and J. Georgy, "Fundamentals of inertial navigation, satellite-based positioning and their integration," 2013.

[6] Wikipedia, "Scooby-Doo — Wikipedia, the free encyclopedia." http://en.wikipedia.org/w/index.php?title=Scooby-Doo&oldid=1066554714, 2021. [Online; accessed 21-September-2021].

[7] Wikipedia, "Orbital elements — Wikipedia, the free encyclopedia." http://en.wikipedia.org/w/index.php?title=Orbital%20elements&oldid=1047400089, 2021. [Online; accessed 30-August-2021].

[8] T. Neilsen, C. Weston, C. Fish, and B. Bingham, "Dice: Challenges of spinning

cubesats," in *37th Annual AAS Guidance and Control Conference, Breckenridge, CO*, 2014.

[9] M. Sweeting, "Modern small satellites-changing the economics of space," *Proceedings of the IEEE*, vol. 106, no. 3, pp. 343–361, 2018.

[10] A. Slavinskis, H. Ehrpais, H. Kuuste, I. Sünter, J. Viru, J. Kütt, E. Kulu, and M. Noorma, "Flight results of estcube-1 attitude determination system," *Journal of Aerospace Engineering*, vol. 29, no. 1, p. 04015014, 2016.

[11] J. L. Crassidis and F. L. Markley, "Unscented filtering for spacecraft attitude estimation," *Journal of Guidance, Control, and Dynamics*, vol. 26, no. 4, pp. 536–542, 2003.

[12] M. L. Psiaki, F. Martel, and P. K. Pal, "Three-axis attitude determination via kalman filtering of magnetometer data," *Journal of Guidance, Control, and Dynamics*, vol. 13, no. 3, pp. 506–514, 1990.

[13] H. E. Soken, "A survey of calibration algorithms for small satellite magnetometers," *Measurement: Journal of the International Measurement Confederation*, vol. 122, pp. 417–423, jul 2018.

[14] J. C. Springmann and J. W. Cutler, "Attitude-Independent Magnetometer Calibration with Time-Varying Bias," *Journal of Guidance, Control, and Dynamics*, vol. 35, no. 4, pp. 1080–1088, 2012.

[15] E. Kim, H. Bang, and S.-H. Lee, "Attitude Independent Magnetometer Calibration Considering Magnetic Torquer Coupling Effect," *Journal of Spacecraft and Rockets*, vol. 48, no. 4, pp. 691–694, 2011.

[16] H. E. Söken and S. Sakai, "Real-Time Attitude-Independent Magnetometer Bias Estimation for Spinning Spacecraft," *Journal of Guidance, Control, and Dynamics*, vol. 41, pp. 276–279, oct 2017.

[17] H. E. Soken, M. E. Cetin, and S.-i. Sakai, "Attitude-independent magnetometer calibration for spinning spacecraft using quasi-measurements," *AAS/AIAA Astrodynamics Specialist Conference*, vol. 501, no. 20, 2020.

[18] J. L. Crassidis, K.-L. Lai, and R. R. Harman, "Real-Time Attitude-Independent Three-Axis Magnetometer Calibration," *Journal of Guidance, Control, and Dynamics*, vol. 28, no. 1, pp. 115–120, 2005.

[19] B. A. Riwanto, T. Tikka, A. Kestila, and J. Praks, "Particle Swarm Optimization with Rotation Axis Fitting for Magnetometer Calibration," *IEEE Transactions on Aerospace and Electronic Systems*, vol. 9251, no. c, pp. 1–1, 2017.

[20] R. Alonso and M. D. Shuster, "TWOSTEP: A fast robust algorithm for attitude-independent magnetometer-bias determination," *Journal of the Astronautical Sciences*, vol. 50, no. 4, pp. 433–451, 2002.

[21] R. Alonso and M. D. Shuster, "Complete linear attitude-independent magnetometer calibration," *Journal of the Astronautical Sciences*, vol. 50, no. 4, pp. 477–490, 2002.

[22] J. Wu, "Real-Time Magnetometer Disturbance Estimation via Online Nonlinear Programming," *IEEE Sensors Journal*, vol. 19, pp. 4405–4411, jun 2019.

[23] S. Sakai, N. Bando, S. Shimizu, Y. Maru, and H. Fuke, "Real-time estimation of the bias error of the magnetometer only with the gyro sensors," in *28th International Symposium on Space Technology and Science*, (Okinawa, Japan), pp. 1–6, 2011.

[24] G. Troni and R. M. Eustice, "Magnetometer bias calibration based on relative angular position: Theory and experimental comparative evaluation," in *2014 IEEE/RSJ International Conference on Intelligent Robots and Systems*, pp. 444–450, IEEE, sep 2014.

[25] G. Fedele, L. D'Alfonso, and G. D'Aquila, "Magnetometer Bias Finite-Time Estimation Using Gyroscope Data," *IEEE Transactions on Aerospace and Electronic Systems*, vol. 54, no. 6, pp. 2926–2936, 2018.

[26] B. Grandvallet, A. Zemouche, M. Boutayeb, and S. Changey, "Real-Time Attitude-Independent Three-Axis Magnetometer Calibration for Spinning Projectiles: A Sliding Window Approach," *IEEE Transactions on Control Systems Technology*, vol. 22, no. 1, pp. 255–264, 2014.

[27] D. Gebre-Egziabher, G. H. Elkaim, J. David Powell, and B. W. Parkinson, "Calibration of strapdown magnetometers in magnetic field domain," *Journal of Aerospace Engineering*, vol. 19, no. 2, pp. 87–102, 2006.

[28] E. Thébault, C. C. Finlay, C. D. Beggan, P. Alken, J. Aubert, O. Barrois, F. Bertrand, T. Bondar, A. Boness, L. Brocco, *et al.*, "International geomagnetic reference field: the 12th generation," *Earth, Planets and Space*, vol. 67, no. 1, pp. 1–19, 2015.

[29] M. D. Shuster *et al.*, "A survey of attitude representations," *Navigation*, vol. 8, no. 9, pp. 439–517, 1993.

[30] B. Gambhir, "Determination of magnetometer biases using module residg algorithm," *Computer Sciences Corporation, Report*, no. 3000-32700, p. 01, 1975.

[31] S. Julier, J. Uhlmann, and H. F. Durrant-Whyte, "A new method for the nonlinear transformation of means and covariances in filters and estimators," *IEEE Transactions on automatic control*, vol. 45, no. 3, pp. 477–482, 2000.

[32] E. A. Wan, R. Van Der Merwe, and S. Haykin, "The unscented kalman filter," *Kalman filtering and neural networks*, vol. 5, no. 2007, pp. 221–280, 2001.

[33] G. H. Golub and C. F. Van Loan, "Matrix computations. edition," 1996.

[34] Z. Zhang, J. Xiong, and J. Jin, "On-orbit real-time magnetometer bias determination for micro-satellites without attitude information," *Chinese Journal of Aeronautics*, vol. 28, no. 5, pp. 1503–1509, 2014.

[35] H. Ersin Soken, S.-I. Sakai, K. Asamura, Y. Nakamura, and T. Takashima, "Spin parameters and nonlinear Kalman Filtering for spinning spacecraft attitude estimation," in *Advances in the Astronautical Sciences*, vol. 160, 2017.

[36] Y. Nakamura, S. Fukuda, Y. Shibano, H. Ogawa, S.-i. Sakai, S. Shimizu, E. Soken, Y. Miyazawa, H. Toyota, A. Kukita, Y. Maru, J. Nakatsuka, T. Sakai, S. Takeuchi, K. Maki, M. Mita, E. Ogawa, Y. Kakehashi, K. Nitta, K. Asamura, T. Takashima, and I. Shinohara, "Exploration of energization and radiation in geospace (ERG): challenges, development, and operation of satellite systems," *Earth, Planets and Space*, vol. 70, no. 102, 2018.

[37] H. E. Soken, S.-i. Sakai, K. Asamura, Y. Nakamura, T. Takashima, and I. Shinohara, “Advanced Attitude Determination Algorithm for Spinning Spacecraft: Preliminary Results with Arase,” *Aerospace*, vol. 7, no. 97, 2020.

[38] B. F. La Scala and R. R. Bitmead, “Design of an extended kalman filter frequency tracker,” *IEEE Transactions on Signal Processing*, vol. 44, no. 3, pp. 739–742, 1996.